Conversion of a Molecular Beam Epitaxy System

for the Growth of 6.1 Angstrom Semiconductors

by

W. Hank G. Dettlaff

A Thesis Presented in Partial Fulfillment
of the Requirements for the Degree
Master of Science

Approved April 2012 by the
Graduate Supervisory Committee:

Yong-Hang Zhang, Chair
Dragica Vasileska
Shane Johnson

ARIZONA STATE UNIVERSITY

May 2012

ABSTRACT

A dual chamber molecular beam epitaxy (MBE) system was rebuilt for the growth of 6.1 Angstrom II-VI and III-V compound semiconductor materials that are to be used in novel optoelectronic devices that take advantage of the nearly continuous bandgap availability between 0 eV and 3.4 eV. These devices include multijunction solar cells and multicolor detectors. The MBE system upgrade involved the conversion of a former III-V chamber for II-VI growth. This required intensive cleaning of the chamber and components to prevent contamination. Special features including valved II-VI sources and the addition of a cold trap allowed for the full system to be baked to 200 degrees Celsius to improve vacuum conditions and reduce background impurity concentrations in epilayers. After the conversion, the system was carefully calibrated and optimized for the growth of ZnSe and ZnTe on GaAs (001) substrates. Material quality was assessed using X-ray diffraction rocking curves. ZnSe layers displayed a trend of improving quality with decreasing growth temperature reaching a minimum full-width half-maximum (FWHM) of 113 arcsec at 278 degrees Celsius. ZnTe epilayer quality increased with growth temperature under Zn rich conditions attaining a FWHM of 84 arcsec at 440 degrees Celsius. RHEED oscillations were successfully observed and used to obtain growth rate in situ for varying flux and temperature levels. For a fixed flux ratio, growth rate decreased with growth temperature as the desorption rate increased. A directly proportional dependence of growth rate on Te flux was observed for Zn rich growth. Furthermore, a

method for determining the flux ratio necessary for attaining the stoichiometric condition was demonstrated.

ACKNOWLEDGMENTS

I wish to extend my deepest gratitude to Dr. Yong-Hang Zhang for his support of my graduate studies at Arizona State University. I truly appreciate the flexibility he afforded me in exploring my interests and the wisdom he shared throughout this time.

I am also grateful to Dr. Shane Johnson and Dr. Dragica Vasileska for being a part of my graduate committee and for the interest they took in my success.

My most sincere thanks also goes out to all members of the ASU MBE Optoelectronics Group without whom the MBE system upgrade would not have been possible. In particular, I cannot thank enough Dr. Ding Ding for his tremendous selflessness during the upgrade; Dr. Stuart Farrell for sharing his time and knowledge during the system calibration; Jin Fan for carrying out the many XRD measurements used in this thesis; and Michael DiNezza for his input on my thesis and for helping with thickness measurements.

Last but not least, I wish to thank my wife, Krista, for her support and patience throughout my Masters and to my parents without whose love and dedication I would not be here today.

TABLE OF CONTENTS

Page

LIST OF TABLES vi

LIST OF FIGURES vii

CHAPTER

1 INTRODUCTION 1

1.1 Background 1

1.2 Overview of Electrical and Optical Properties 2

1.3 Proposed Applications 3

1.3.1 Multijunction Solar Cells 4

1.3.2 Multicolor Photodetectors 7

1.3.3 Other Proposed Applications 10

1.4 Prior Work 11

2 FACILITIES DEVELOPMENT 12

2.1 Growth System Requirements 12

2.2 Basics of Molecular Beam Epitaxy 13

2.3 II-VI and III-V Dual Chamber Features 17

2.3.1 Chamber Layout 17

2.3.2 Vacuum System 20

2.3.3 Sources for 6.1 Å II-VI and III-V Materials Growth 22

2.3.4 In-situ Monitoring Systems 24

2.3.5 Computer Control 27

2.4 System Upgrade Process 28

CHAPTER Page

2.4.1 Preparation for System Cleaning 28

2.4.2 Chamber Cleaning 29

2.4.3 High Temperature II-VI Chamber Bake 30

2.4.4 Component Maintenance and Replacement........ 34

2.4.5 Full System Bake 36

3 GROWTH CALIBRATION FOR II-VI SEMICONDUCTORS 39

3.1 Growth Preparation 39

3.1.1 Substrate Mounting 39

3.1.2 As-Free GaAs Substrate Deoxidation 44

3.2 Source Flux Calibration 47

3.3 ZnSe Growth Calibration 51

3.4 ZnTe Calibration 55

3.4.1 Growth Condition Experimentation 55

3.4.2 RHEED Oscillation Growth Rate Study 60

4 SUMMARY AND CONCLUSIONS 68

REFERENCES 72

LIST OF TABLES

Table Page

1.1: Electron and hole mobilities at 300 K for binaries with lattice constants near 6.1 Å.......... 3

1.2: Layer structure for four junction solar cell.......... 6

3.1: Fluxes resulting in stoichiometric adsorption with corresponding Te/Zn ratio 66

LIST OF FIGURES

Figure Page

1.1: Bandgap versus lattice constant for various III-V and II-VI semiconductor alloys (Courtesy: D. Ding) 2

1.2: Optically addressed two terminal photodetector schematic [**8**]. 8

1.3: Individual photodiode spectral responsivity curves [**8**]. 9

1.4: InGaP photodiode linear dynamic range with different light bias levels for inactive photodiodes [**8**]. 9

2.1: Basic MBE system schematic. 14

2.2: II-VI and III-V dual chamber system (Courtesy: D. Ding). 17

2.3: II-VI and III-V isolation plan for wafer holder stages. 18

2.4: RHEED images before (a) and after (b) As cap layer removal. 20

2.5: II-VI chamber source setup (Courtesy: D. Ding). 22

2.6: III-V chamber source setup (Courtesy: D. Ding) 22

2.7: II-VI valve schematic. 24

2.8: II-VI chamber high temperature baking setup (Courtesy: D. Ding) 31

2.9: II-VI chamber pressure and temperatures versus baking time. 32

2.10: RGA partial pressure scans of the III-V chamber (main) and II-VI chamber post-bake (inset). 33

2.11: Partial pressures versus time recorded at cold trap during bake. 36

2.12: Analog RGA scans at the cold trap before and after bake. 37

3.1: Schematic of a full-wafer holder. 40

Figure Page

3.2: DRS temperature vs. thermocouple temperature for substrates of different lots mounted with In-free wafer holders under equilibrium (solid line segments) and fast positive ramp (solid line segments). 41

3.3 DRS temperature versus thermocouple temperature for substrates of different lots using In mounting. 43

3.4: (2×1) RHEED pattern of GaAs (001) substrate at a peak deoxidation temperature of 620 °C (DRS). 46

3.5: Zn flux versus source temperature. 47

3.6: Se flux versus source temperature. 48

3.7: Te flux versus source temperature. 48

3.8: Se flux versus valve position for Se cell bulk temperature of 200 °C. 49

3.9: Te flux versus valve position 50

3.10: RHEED reconstructions for (a) [110] azimuth and for (b) [100] azimuth near the stoichiometric condition. 52

3.11: XRD ω-2θ FWHM versus substrate temperature of ZnSe samples grown using standard deoxidation procedure and low temperature As cap desorption. 54

3.12: RHEED images for Te to Zn ratios of 1.46:1 (a, b) and 1.26:1 (c, d) in [110] azimuth (a, c) and [100] azimuth (b, d). 56

3.13: XRD ω-2θ FWHM versus substrate temperature for ZnTe samples. 57

3.14: Measured XRD ω-2θ FWHM and thickness broadening adjusted FWHM versus thickness of ZnTe samples. 58

Figure Page

3.15: Growth rate versus measured flux ratio for ZnTe samples.......................... 59

3.16: Example of RHEED oscillation obtained during ZnTe growth rate study with fitted damped sine wave. 61

3.17: RHEED oscillation displaying double peak due to a misaligned electron beam. 62

3.18: Growth rate versus substrate temperature for various Te valve. Desorption rate also shown. 63

3.19: Growth rate versus Te valve position cross-section of Figure 3.18 at 418 °C superimposed on flux versus Te valve position from Figure 3.9................. 64

3.20: Growth rate versus measured Te flux for various Zn source fluxes. 65

1 INTRODUCTION

1.1 Background

It has long been a goal of the optoelectronics community to integrate a wide range of devices onto a single substrate. Presently, this has been a challenge as a wide array of materials and substrates are enlisted in order to cover even the most common spectral ranges while maintaining the required level of material quality. For example, UV detectors are grown on GaN and sapphire substrates; infrared photodetectors use InP substrates; blue InGaN LEDs are grown on GaN substrates; and red AlGaInP LEDs utilize GaAs substrates.

While there has been a significant amount of research into the hybrid integration of existing materials systems, there is yet to be a universal solution that would enable a wide range of devices to be practically integrated onto a single substrate. A new materials platform involving II-VI and III-V semiconductors lattice matched to GaSb and InAs substrates has been recently proposed to address this [**1**]. This system features semiconductor binaries and related alloys with direct bandgaps ranging from nearly 0 eV (far infrared) to 3.4 eV (ultraviolet). In turn, this 6.1 Å lattice matched II-VI and III-V materials platform makes the dream of integrating a wide range of photonic devices onto a single substrate highly plausible.

1.2 Overview of Electrical and Optical Properties

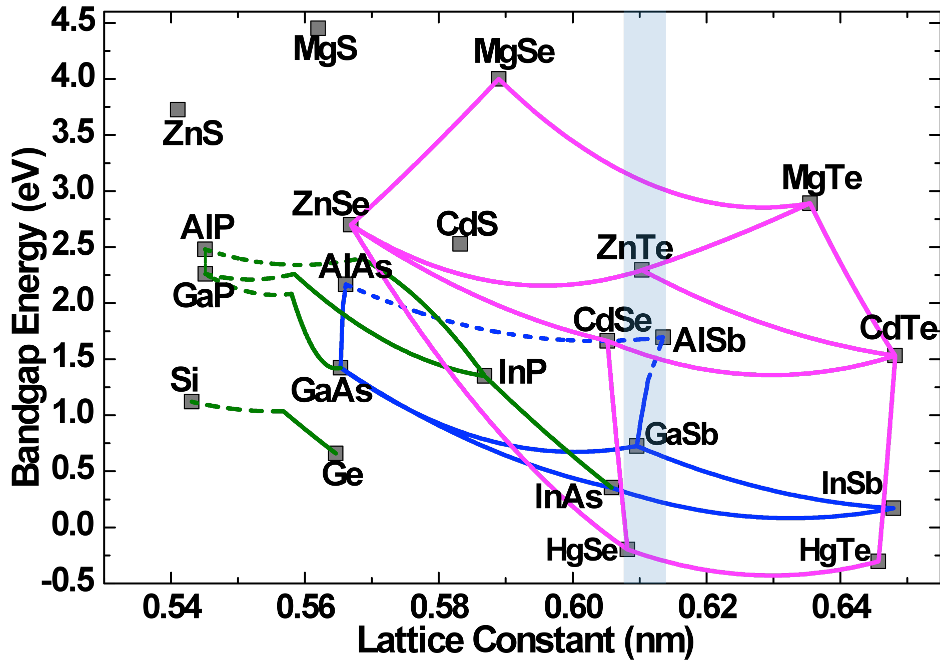

Figure 1.1: Bandgap versus lattice constant for various III-V and II-VI semiconductor alloys (Courtesy: D. Ding)

As was aforementioned, the 6.1 Å lattice matched II-VI and III-V materials platform spans the electromagnetic spectrum from around 0 eV up to 3.4 eV. This is achieved with alloys using up to four constituents. Figure 1.1 displays the bandgap versus lattice constant for a number of binary and ternary semiconductor compounds. It is important to note that not only are energy levels in this range attainable but also that a majority of the alloys used are direct bandgap.

The 6.1 Å lattice matched II-VI and III-V material platform also has competitive electrical properties. Electron and hole mobilities are listed for a selection of binaries with lattice constants near 6.1 Å in Table 1.1. GaSb and InAs

have very high mobilities and would be well suited for use as conduction channels. As expected, the materials with larger bandgaps and greater effective masses have reduced mobilities making them better suited for electrical barrier and optical confinement layers. Overall, the near 6.1 Å binaries offer comparable or better mobilities then those of similar bandgap and different lattice constant.

Table 1.1: Electron and hole mobilities at 300 K for binaries with lattice constants near 6.1 Å.

Material	Electron Mobility (cm^2/V s)	Hole Mobility (cm^2/V s)
ZnTe	600	100
CdSe	900	50
AlSb	200	420
GaSb	12040	1624
InAs	30000	450

1.3 Proposed Applications

A wide range of photonic and electronic devices with minimal misfit dislocations grown on GaSb or InAs substrates can be envisioned by using the 6.1 Å materials platform. Of particular interest are those utilizing the ability to monolithically integrate a range of lattice-matched materials with bandgaps spanning a large portion of the electromagnetic spectrum. This level of freedom in device design is not known to be available for any other existing material system that is lattice matched to a single substrate. Successful development of the monolithically integrated device structures will open the door to additional

innovative device concepts and higher levels of system integration. Two such device applications—multijunction solar cells and multicolor photodetectors—are discussed in depth in the following.

1.3.1 *Multijunction Solar Cells*

In recent years, concerns pertaining to the limited supply and environmental effects of various traditional energy sources such as oil and coal have been increasing. Consequently, the desire to find viable alternative energy resources has risen as well. The use of solar cells to convert sunlight directly into electricity via the photovoltaic effect is one possible solution. However, a variety of challenges have yet to be addressed before this technology will be competitive with traditional sources. These include electric infrastructure issues, energy storage, and cost reduction.

When addressing economic issues, the cost of the module and installation must be considered in addition to that of the photovoltaic device and materials. For market dominating Silicon based solar cells, 60 to 75 percent of module cost is due to the cell component itself. With only minimal reductions in cost expected and efficiencies nearing theoretical limits for these cells, it is clear that solutions minimizing the cell component cost while allowing for increased efficiency would be extremely advantageous. This can be addressed by using potentially comparably inexpensive concentrator systems at ratios reaching over 1000, vastly reducing the cell component size and material requirements.

With the proportion of cell component cost drastically reduced, it is advantageous to use higher efficiency cells that can be better tuned for high

concentration ratios. The framework for increasing efficiency by using multiple energy gaps was laid out by Henry's extension of the Shockley-Queisser detailed balance limit for pn junction solar cells [**2**,**3**]. By using multiple junctions, a better fit to the solar spectrum can be attained by minimizing unabsorbed photons that are at energies below the bandgap and by minimizing energy losses due to the position of hot carriers created by photons of energies exceeding the bandgap. Additionally, since current is reduced with increased junctions, losses due to series resistance are also reduced allowing the theoretical limits to be more closely approached. As a result of these advantages, multijunction cells have held the efficiency records for nearly two decades reaching as high as 43.5% under concentration[**4**].

These state-of-the art cells have primarily been grown on GaAs and Ge substrates. Unfortunately, significant efficiency increases have been hindered due to a lack of high quality, lattice-matched materials in the 1.0 eV to 1.3 eV bandgap range. These are necessary for increasing efficiency through increased junctions. [**5**]. The use of metamorphic buffer layers have shown some promise in alleviating these issues however production costs and cell longevity issues associated with resulting defects are major concerns [**5**,**6**]. Consequently, the ideal path forward requires lattice-matched materials over a wide range of desired bandgap energies. The 6.1 Å II-VI and III-V materials platform provides these features [**1**].

A number of additional advantages are enabled by this platform. Beyond covering the 1.0 eV to 1.3 eV gap associated with materials matched to GaAs and

Ge, the (InAlGa)(AsSb) alloys in this platform reach further into the infrared spectrum. This is especially advantageous for increasing efficiency under very high solar concentrations. Furthermore, the direct-indirect band crossover of the AlGaAsSb alloys included in the platform promotes a unique combination of high absorption, long carrier lifetimes, and increased V_{oc} [**1**]. Finally, available type-II heterostructures are expected to allow tunnel junction designs with extremely low voltage drops. This feature will be extremely important in taking full advantage of high concentration ratios.

Table 1.2: Layer structure for four junction solar cell.

Material	Bandgap (eV)	Thickness (μm)
$Zn_{0.76}Cd_{0.24}Se_{0.23}Te_{0.77}$	2.04	1.20
$CdSe_{0.90}Te_{0.10}$	1.56	1.30
$Al_{0.32}Ga_{0.78}As_{0.03}Sb_{0.97}$	1.21	2.10
$Al_{0.13}Ga_{0.87}As_{0.01}Sb_{0.99}$	0.92	2.50

A variety of potential solar cell structures have been investigated using Silvaco simulation software. Simulated efficiencies as high as 54% under 1000 suns using the AM1.5D spectrum result using the structure shown in Table 1.2 [**7**]. These simulations show great promise for the use of the 6.1 Å II-VI and III-V materials platform in record efficiency multijunction solar cells. The successful growth of these structures requires the ability to grow both II-VI and III-V alloys while maintaining high quality interfaces and avoiding unintentional dopants.

Consequently, these and related solar cell structures are a major motivator for the MBE upgrade discussed within this thesis.

1.3.2 *Multicolor Photodetectors*

The wide spectrum coverage enabled by the 6.1 Å II-VI and III-V materials platform has advantages for applications beyond solar cells. It could also provide a new level of flexibility for monolithically integrating photodiodes of multiple bandgaps onto a single substrate. This feature has potential application in imaging, environmental monitoring, communications, and spectroscopy [**8**].

The ability to integrate many detection bands onto a single substrate introduces system design challenges. With existing solutions, the maximum amount of detection bands possible using a single read out integrated circuit (ROIC) is two [**9**]. This can be accomplished using voltage biasing with photodiodes in a back-to-back configuration [**10**,**11**]. Alternatively, the two-band limit can be surpassed by incorporating additional terminals [**12**,**13**,**14**]. However, this incurs tradeoffs as the focal plane array layout becomes more complex, fabrication becomes significantly more difficult, ROIC requirements are increased, and fill factor is reduced [**15**]. In turn, these problems are inhibitive for increasing detection bands.

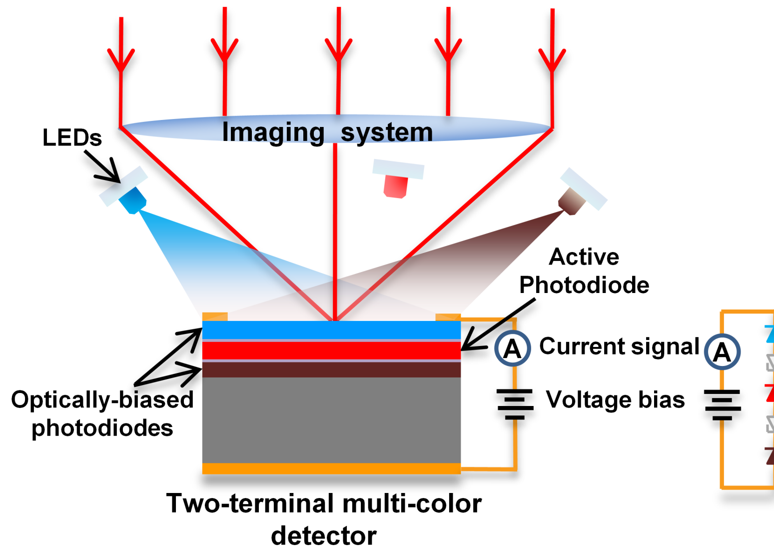

Figure 1.2: Optically addressed two terminal photodetector schematic [**8**].

In order to maximize the potential of the 6.1 Å materials platform, a two terminal solution allowing an almost limitless number of bands has been proposed [**8**]. This would utilize the concept of current limiting. Whereas in solar cells it creates challenges for maximizing efficiency, it is advantageous for measuring only the current of the desired cell in this case. In order to read a particular photodiode, all other photodiodes in the monolithically grown stack are light biased with an LED or laser within their respective spectral response ranges. The photogenerated current of the cell of interest then dictates that of the overall multicolor detector given it does not exceed that of the optically biased cells. Hence, by switching the appropriate light bias sources a single ROIC can be used to detect in any number of available bands.

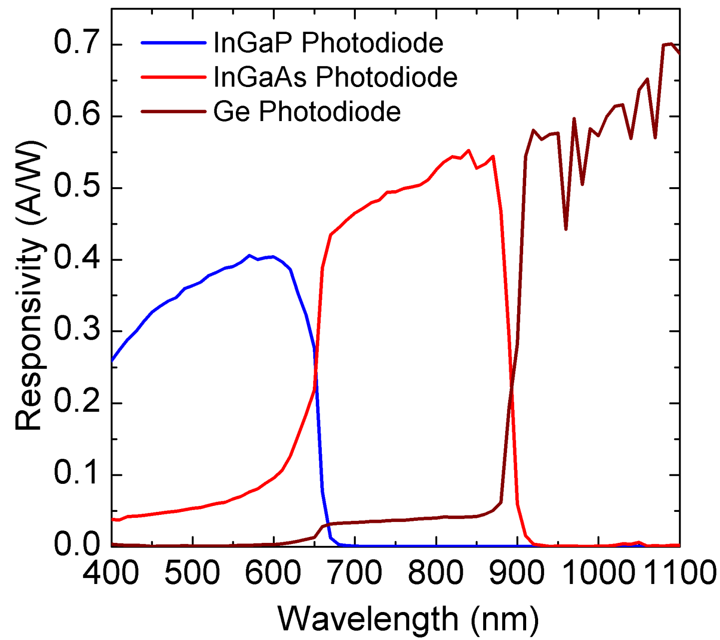

Figure 1.3: Individual photodiode spectral responsivity curves [**8**].

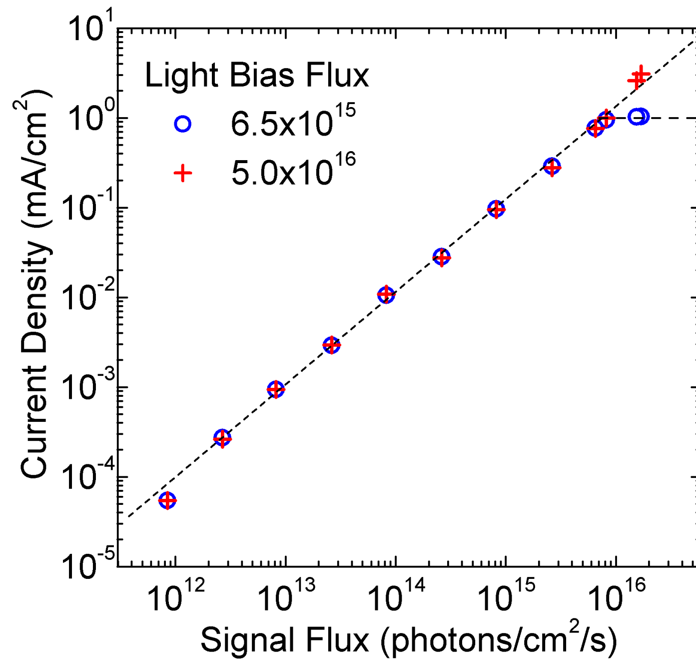

Figure 1.4: InGaP photodiode linear dynamic range with different light bias levels for inactive photodiodes [**8**].

This concept has been experimentally demonstrated [**8**]. Due to the inherent structural similarity and immediate availability, a commercial InGaP/InGaAs/Ge triple-junction solar cell was used as a multicolor photodetector for the study. Optical biasing was achieved using LEDs with peak wavelengths within the response ranges of each junction of the solar cell. Using the biasing method described earlier, responsivity plots were obtained (Figure 1.3) confirming that photodiodes can be addressed individually. It is believed that the responses noted outside the desired range of the InGaAs and Ge cells can be overcome with design modifications. Reasonably high linear dynamic range was also demonstrated (Figure 1.1). These results are promising for future development of the concept and its extension into utilizing the 6.1 Å lattice-matched materials system to achieve detectors with many detection bands and only two terminals.

1.3.3 *Other Proposed Applications*

The 6.1 Å II-VI and III-V materials platform may also offer solutions for a number of other optoelectronic applications. One example is within the development of high efficiency LEDs. Within the range of 540 nm to 610 nm, a number of efficiency limiting problems have been encountered using conventional materials. ZnTe has the potential to address this as its bandgap corresponds to an emission wavelength of 546 nm [**16**]. The wide range of bandgaps achievable with this system also has the potential to facilitate broad integration of electronic and optoelectronic devices onto a single substrate. In addition to spectral properties, the variety of band alignments available within the

system may be useful for a number of innovative optical and electrical confinement structures.

1.4 Prior Work

The success of the proposed devices is contingent on the ability to integrate II-VI and III-V materials while maintaining low defect densities. Since GaSb is the preferred substrate for its available sizes and comparably low cost, initial studies have involved the growth of ZnTe on this material. In a work by Wang et al [**17**], thin layers of ZnTe were grown on GaSb substrates and were characterized by X-ray diffraction (XRD) and transmission electron microscopy (TEM). The ω-2θ XRD scans displayed distinct epilayer and substrate peaks as well as Pendellösung fringes. These fringes indicate that the epitaxial layer has a smooth interface, uniform thickness, and low defect density. This was confirmed with TEM images that displayed an interface free from misfit dislocations or stacking faults. This study also included the growth of a ZnCdTe/ZnTe quantum well on a GaSb substrate. Photoluminescence measurements detected strong emission. These findings indicate that low defect density interfaces for the II-VI and III-V materials platform are realistically attainable.

Fan et al [**18**] offer further confirmation of this for thicker ZnTe layers. In this work, excellent XRD FWHM values as low as 32.9 arcsec were obtained for a 2.5 μm layer on GaSb. Strong PL spectra were noted as well. Growth of ZnTe on GaAs substrates was also studied. FWHM values as low as 45.0 arcsec were obtained for these samples. Since GaAs substrates were used for the calibration of the rebuilt chamber, these values served as an excellent reference level.

2 FACILITIES DEVELOPMENT

2.1 Growth System Requirements

The 6.1 Å lattice-matched materials platform and its previously discussed applications come with unique challenges and constraints for achieving successful growth. The foremost of these is the avoidance of cross contamination between II-VI and III-V sources. This is because the constituents of each alloy group can contribute to unintended doping in the other. For example, As acts as an acceptor to ZnTe by replacing Te sites [**19**]. Likewise, Te is commonly used to dope III-V materials n-type. In order to attain desired device performance, unintentional doping from each alloy type must be minimized to achieve specified doping levels.

The various applications listed in the introduction include features that are challenging for growth. Thin layers around 10 nanometers are required for the tunnel junctions utilized by both multijunction solar cells and multicolor detectors. Even thinner layers are sometimes utilized in superlattices and quantum wells. Moreover, abrupt interfaces between these layers are usually desired. Given that the lattice constant of most semiconductors is between 0.54 nm and 0.65 nm, the growth method employed must be able to produces layers with monolayer accuracy.

The nearly continuous range of bandgaps enabled by the 6.1 Å lattice-matched materials platform is only possible with careful compositional control of alloys with up to four constituents. Many of these alloys are in the miscibility gap of techniques that rely on chemical processes that require near equilibrium growth

conditions. As a result, a technique that is not primarily dictated by these processes is desired. In summary, the desired technique must achieve the following: cross contamination minimization; precise layer thickness control; precise alloy composition control; and nonequilibrium growth.

MBE is the solution that best meets these constraints. With specialized system setup, the minimization of cross contamination is possible as will be discussed in detail throughout the remainder of this chapter. The growth processes intrinsically associated with MBE address the latter challenges and are in the immediately following section. It should be noted that metalorganic chemical vapor deposition (MOCVD) is a suitable alternative for creating the discussed devices in most cases. This is important for commercialization as its higher throughput is preferable for industrial device production. Due to the comparable ease of altering growth conditions and higher level of control, MBE is the preferred method for research purposes.

2.2 Basics of Molecular Beam Epitaxy

Fundamentally, MBE [**20**,**21**] is the growth of thin films formed by the interaction of atomic or molecular beams with a substrate. By balancing the arrival rate of constituent atoms in these beams with the temperature of the substrate, a level of surface migration is achieved that results in very smooth surfaces. Consequently, a level of control is enabled where deposition can be started and stopped within a monolayer and the growth of the thin layers necessary for the previously discussed applications is possible.

The low growth rates employed further assist in the control of material composition. What truly makes MBE the optimal choice in this sense is its ability to achieve nonequilibrium growth. Other growth techniques such as liquid phase epitaxy and vapor phase epitaxy rely on chemical processes that require conditions near thermodynamic equilibrium vastly limiting the compositions achievable. MBE growth, however, is governed primarily by the kinetics of incoming atoms and molecules effectively removing most of these limitations. This is the enabling feature for attaining nearly continuous bandgap coverage in the 6.1 Å II-VI and III-V materials platform.

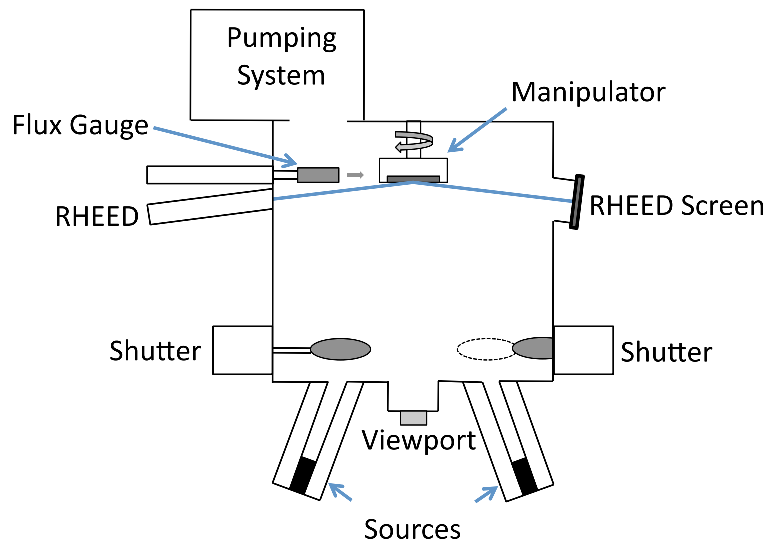

Figure 2.1: Basic MBE system schematic.

The basic physical setup used to foster high quality MBE growth is now discussed (Figure 2.1). The first step is to create an environment that minimizes incorporation of unintended materials. Limitations imposed by the control system and growth processes dictate growth rates of approximately 1 monolayer per

second. The impingement rate necessary for this amounts to a partial pressure on the order of 10^{-6} Torr corresponding to a mean free path in the range of meters to tens of meters. Since negligible interactions occur prior to reaching the substrate, the physical growth mode discussed previously is enabled. In order to achieve acceptable impurity levels, for example 1 atom in 10^{8}, a background vacuum level of approximately 10^{-14} Torr would be needed. Fortunately, this is requirement is lessened by typically low impurity sticking coefficients. Consequently, background pressures of 10^{-9} Torr have proven to be acceptable.

Achieving the necessary ultra-high vacuum (UHV) requires special care for the build and design of all portions of the system. This starts with a stainless steel chamber evacuated by a complement of pumps. The selection of pumps in the II-VI and III-V dual chamber system will be discussed in Section 2.3.2. In most systems, these primary pumps are supplemented by a cryopanel that surrounds the deposition region. These serve the dual purpose of absorbing stray radiation from various heaters and acting as a secondary pump to minimize stray flux. The maintenance of this vacuum and the minimization of external impurity introduction are assisted by the use of a load lock and preparation chamber connected to the growth chamber via gate valves. Respectively, these are used for introducing substrates from atmosphere and outgassing contaminants from substrates.

In addition to providing the proper environmental conditions, MBE systems must also deliver and control the constituent materials used for the growth. A variety of methods are used for flux generation including thermal

effusion sources, gas sources, and electron beam evaporation sources. The most commonly used of these and that employed by the II-VI and III-V chambers is the thermal effusion cell. In these cells, source material is radiatively heated resulting in evaporation. Flux is directly related to source temperature and hence closely tied to crucible temperature. By using a flux measurement device such as an ionization gauge, calibration curves can be attained enabling control using simple temperature controllers. A variety of modifications are possible to make these sources more suitable for certain materials and to add a higher level of flux control. Those applicable to the ASU system will be described in Section 2.3.3.

In order to grow a variety of materials, a typical chamber will have multiple sources. Mechanical shutters are used with each of these to facilitate sub-monolayer interruption of flux enabling abrupt interfaces between layers. Accommodating multiple sources requires that they be setup at an angle to the substrate normal. This leads to a non-uniform flux profile at the substrate surface. Substrate rotation is employed to effectively average flux and ensure an even growth profile across the substrate. This feature is incorporated into a component referred to as the manipulator which also serves roles in substrate temperature control and wafer transfer.

Successful growth, of course, requires sufficient in situ control, measurement, and analysis inside the MBE chambers. Sources and substrates must be equipped with temperature measurement devices. Along with shutters and other components, these are usually interfaced with some sort of computer control. Additional ports are often included to facilitate additional growth

monitoring. The UHV environment provides advantages compared to many other growth methods in that many in situ monitoring systems such as reflection high energy electron diffraction (RHEED) can be used.

2.3 II-VI and III-V Dual Chamber Features

The integration of II-VI and III-V materials presents many challenges as have been discussed previously. Specialized setup and procedures must be implemented to minimize cross contamination. Additionally, certain properties of II-VI materials require additional care in component selection. The system design measures taken to facilitate the high quality growth of II-VI and III-V integrated devices are discussed in the following.

2.3.1 *Chamber Layout*

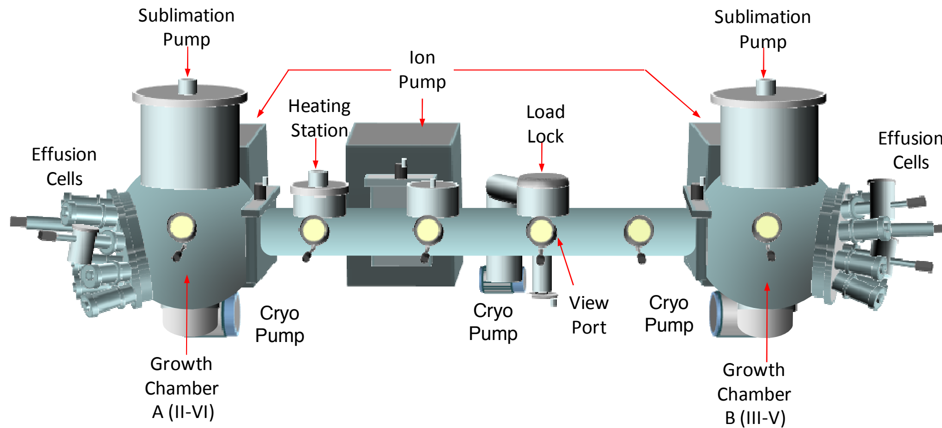

Figure 2.2: II-VI and III-V dual chamber system (Courtesy: D. Ding).

The II-VI and III-V MBE machine was built upon what was originally a VG V80H dual III-V chamber system. A schematic of the modified system is shown in Figure 2.2. Each growth chamber is connected by a dual-purpose transfer and preparation chamber. Substrates are loaded into this chamber via a

fast entry load lock chamber. As standard operating procedure, the gate valve between the growth and preparation chamber and the seal between preparation chamber and load lock are never opened simultaneously. This provides an additional stage of isolation of growth chambers from atmospheric conditions. Additionally, after loading the substrate, a high temperature heating stage in the preparation chamber is used to outgas contaminants.

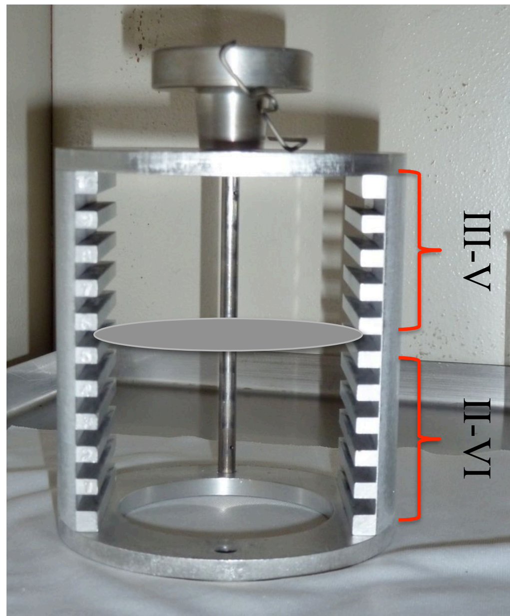

Figure 2.3: II-VI and III-V isolation plan for wafer holder stages.

The isolation of II-VI and III-V materials begins with a similar procedure. The gate valves for each growth chamber are never opened simultaneously to minimize the possibility of direct diffusion of contaminating gasses from chamber to chamber. Direct material transfer between chambers must also be minimized. The machine has two wafer stages, one for loading into the preparation chamber from the load lock (Figure 2.3) and one for holding wafers in this chamber. Each has designated locations for wafer holders that are used exclusively in each

chamber with a blank disc placed between the II-VI and III-V sections. This aims to prevent material transfer between chambers via being knocked off during the transfer process or from being outgassed as the wafer is heated up in the growth chamber. This setup, however, requires the wafer to be removed from the system when transferring. In order to prevent surface oxidation, a very thin layer, on the order of monolayers, of low temperature amorphous material can be grown as a barrier. After transferring wafer holders, this layer can then be outgassed in the high temperature stage. Initial tests of this process were promising as shown by RHEED images before and after (Figure 2.4). During the before image, weak spots and hazy RHEED are consistent with a layer of amorphous As material on the surface. After the removal procedure, the background is cleared and the spot intensity increases suggesting the layer is no longer present.

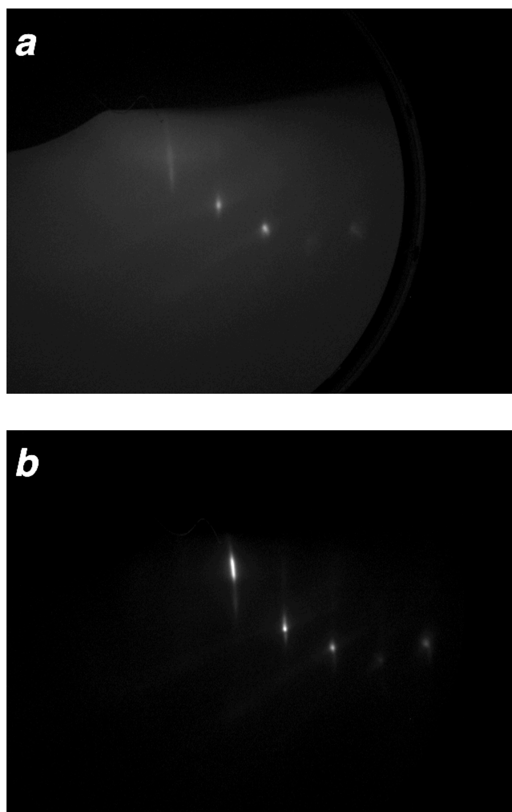

Figure 2.4: RHEED images before (a) and after (b) As cap layer removal.

2.3.2 *Vacuum System*

The system UHV conditions are provided by a relatively common complement of pumps [**22**]. Initial pumping from atmosphere is provided by a turbomolecular pumping station connected via valves to each chamber. This consists of a turbomolecular pump backed by a UHV compatible oil-free roughing pump. This system is optimal as it provides high speed pumping of most gases during pump down and is capable of reaching pressures as low as 10^{-7} Torr.

A cryopump and ion pump pairing provide primary pumping of the chambers. The former is advantageous for its high pumping speeds of atmoshpheric gases and H_2O and high maximum operating pressure. The latter is

highly desired for its reliability and bakeability. Each of these pumps features a gate valve allowing it to be separated from the chamber. This provides both a security measure against pump failure and pump saturation during higher pressure operations. A sublimation pump is utilized as added support on the growth chambers. This uses evaporated titanium to getter gases helping to provide additional pumping speed during growth and to help lower the standby pressure. Additionally, the previously discussed cryopanel is used extensively to provide additional pumping assistance during growth.

The II-VI chamber features the addition of a cold trap connected to its ion pump. This is one of many steps taken to facilitate the unique ability to carry out high temperature (up to 200 °C) bake-outs of the chamber. By maintaining a significantly lower temperature then the chamber, the cold trap will prevent low vapor pressure II-VI materials from condensing on chamber walls during a bake. Periodic use of this of this ability is crucial in maintaining a level of system cleanliness required for the successful growth of high quality devices. The other measures taken to allow this will be discussed in subsequent sections.

The vacuum is monitored in each chamber of the system via Stabil-Ion 360 Series ion gauges. The ion pumps serve as secondary gauges due to the relation of ion pump operating current and pressure. Stanford Research Systems RGA300 residual gas analysis systems fitted to each chamber enable the identification and partial pressure measurement of gases present in the system. This ability finds application in many aspects of MBE including maintenance, growth preparation, and growth.

2.3.3 *Sources for 6.1 Å II-VI and III-V Materials Growth*

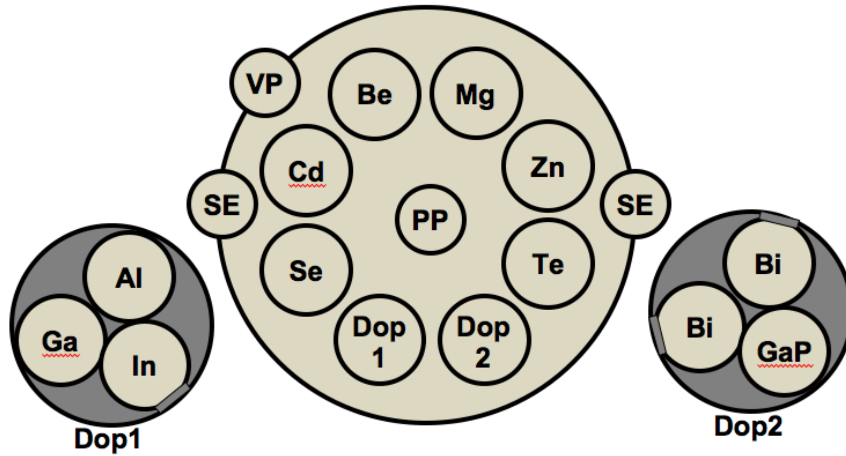

Figure 2.5: II-VI chamber source setup (Courtesy: D. Ding).

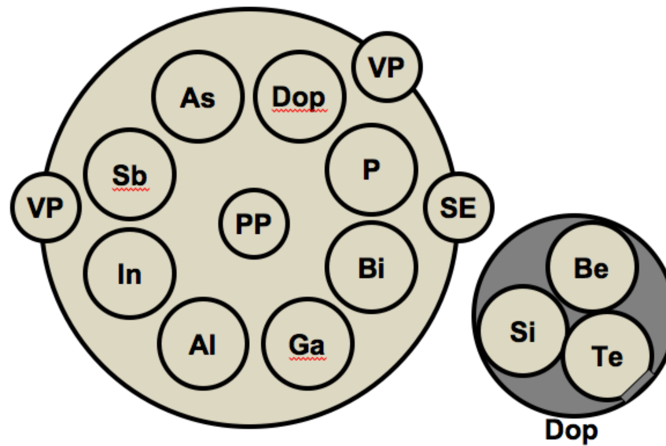

Figure 2.6: III-V chamber source setup (Courtesy: D. Ding)

The sources in the updated system were chosen to provide a wide spectrum of bandgaps through the use of materials that can be lattice matched to 6.1 Å substrates (Figure 1.1). The II-VI chamber utilizes the materials displayed in Figure 2.5. Mg, Se, and Te can be used in a ternary alloys with bandgaps up to 3.4 eV. Exchanging Mg for Cd produces an alloy with the lowest attainable bandgap using the II-VI materials used in the chamber, approximately 1.5 eV.

Similarly, Zn pairs with Te to provide a binary with a bandgap in the middle of the aforementioned ternary alloys.

In the III-V chamber (Figure 2.6), Al and Sb combine to form an alloy with a bandgap of 1.6 eV, slightly overlapping the range of the II-VI chamber materials. The addition of varying amounts of Ga results in lattice matched materials covering the spectrum between the AlSb and the bandgap of GaSb, 0.7 eV. The In and As cells can be used along with Sb to achieve a ternary alloy with a bandgap of approximately 0.4 eV.

Ga, In, and Al are used on the II-VI chamber as n-type dopants. For p-type, a nitrogen source is used as well as a GaP source, from which the desired phosphorous dopant is preferentially evaporated. In the III-V chamber, Be and Si are used for p-type doping while Si and Te are used for n-type doping.

Bi has been included on both chambers because its large size promotes surfactant behavior. This property can be utilized to prevent surface roughening during the growth of various heterostructures and also to modify the mode of growth [**23**]. On the III-V chamber, it can be incorporated with Ga and As to achieve large reductions in bandgap energy with comparably small changes in lattice constant [**24**].

In order to better accommodate the low vapor pressure II-VI materials, specially designed sources with two-piece graphite crucibles were selected. As compared to commonly used crucible material pyrolytic boron nitride (pBN), graphite allows for greater flexibility and higher machining tolerances. This enables the two-piece design that enhances the material loading process. It also

facilitates the customization of source nozzles. This allows smaller apertures to be used to promote higher cell temperatures and better flux control. Moreover, improved flux output profiles are possible.

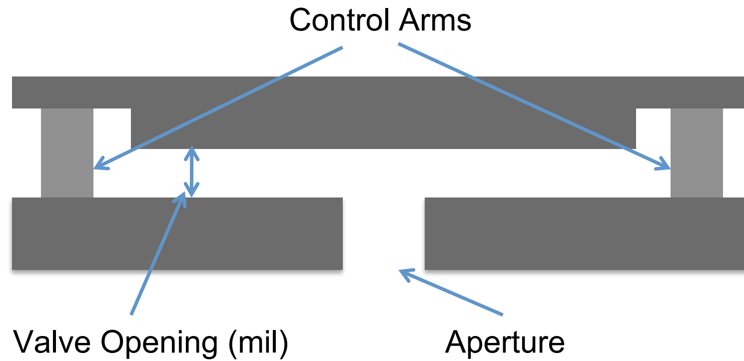

Figure 2.7: II-VI valve schematic.

The Te and Se cells incorporate one further feature to improve their flux control and facilitate higher temperature bakes then have previously been possible on II-VI systems. This is the inclusion of a source valve (Figure 2.7). By using high precision control of the valve opening near instantaneous changes in flux are possible. By closing the valve, negligible source material can be lost thus enabling higher bake temperatures. In order to prevent material deposits on this area, a higher temperature then the crucible is maintained at all times.

2.3.4 *In-situ Monitoring Systems*

Successful MBE growth requires the ability to carefully control growth conditions and monitor growth process. The most fundamental growth conditions are the constituent flux rates and substrate surface temperature. With the flux rates dictated primarily by effusion cell temperature, temperature control is at the heart of attaining desired growth conditions. In each cell, a thermocouple is in contact

with the crucible. Similarly, a thermocouple is used to measure the substrate temperature. However, due to the desire to use In-free mounting and the use of substrate rotation the thermocouple is placed between the wafer and heater. Each of these thermocouples is connected to a PID controller with the corresponding source or substrate heater as its output. This provides the first level of control.

Neither the source or substrate temperature measurements are perfectly stable or accurate. In the sources, the thermal transfer characteristics between the evaporating material and the thermocouple change as material is used. Furthermore, some lag can occur between the measured and actual temperatures. As a result, a flux gauge is used to calibrate the required temperatures more directly and to characterize transient behavior. In the II-VI and III-V dual chamber system, the manipulator can be tilted out of the way so that an ion gauge can be moved into the substrate growth position to provide these functions.

The aforementioned substrate temperature measurement setup tends to be very inaccurate. This is due to the reliance on radiative coupling between the substrate, heater, and the thermocouple. Resultantly, lag is an issue in transient situations. Additionally, temperature offsets vary significantly between different substrates and substrate holders as well. For these reasons, the thermocouple measurements are supplemented with optical measurement methods. In the III-V chamber, an infrared pyrometer with a range of 400 °C to 1200 °C is utilized. This infers the substrate temperature via applying the Stefan-Boltzmann law to the measured thermal radiation.

Since the low growth temperatures used for II-VI growth are out of the specified range of the pyrometer, diffuse reflectance spectroscopy (DRS) is used as an alternative. In this method [**25**], a broadband white light source is focused over the substrate. This passes through the substrate and is diffusely reflected back through the substrate. The spectrum at a nonspecular point is measured using a monochromator. Only light not absorbed in the substrate is measured at this point in turn enabling determination of the bandgap. This can then be used to infer the substrate temperature. If the bandgap-substrate temperature relation is available, this is a highly accurate and robust method. Fortunately, it is well characterized for the GaAs substrates used for the chamber calibration.

As a complement to the growth monitoring systems, RHEED enables the in-situ analysis of epitaxial layer growth. This technique utilizes an electron beam at a glancing angle. At the electron energies used, the beam penetration is typically limited to a few monolayers. This results in a surface sensitive diffraction pattern that can provide many insights into the growth process [**20**].

Both chambers of the II-VI and III-V dual chamber system implement a Staib Instruments RH-15 RHEED system. This features a compact electron gun with an accelerating voltage of 15 keV. The compact geometry is an important feature as it accommodates the baking box necessary for maintaining system cleanliness. The accompanying Staib Instruments kSA400 software enables computer based RHEED image capture and analysis. Of note is the RHEED oscillation tracking and subsequent fitting. This allows for growth rate determination during growth, a key feature for the system calibration.

2.3.5 *Computer Control*

It is clear that the control of MBE involves many inputs including substrate and source temperature controllers, source valves, and shutters. Even for simple structures, the required operator attention can take away from the ability to carefully monitor growth progress. More complex structures may not be able to be grown accurately via manual control. For this reason, both chambers feature high performance computers operating the Emeralt control system. The heart of this system is desktop software that utilizes C-language based input. This allows growth procedures to be programmed in advance. Operator error is minimized and focus can be shifted to monitoring RHEED, DRS temperature, and the substrate. Furthermore, the source temperature ramps can be written as calculation loops simplifying the implementation of graded layers.

An important aspect of the Emeralt system is its real-time control. By supervising execution time, it is ensured that commands will occur at the designated times and not accumulate errors related to computer processing time as can happen in many other control systems. Furthermore, this facilitates the ability to run both parallel and synchronized processes. In turn, growth structures can be executed with a high level of confidence.

Communication in this system is achieved via the TCP/IP ethernet protocol with components selected to minimize latency between computer commands and device action. A bank of TCP/IP to RS-232 controllers is utilized to accommodate older temperature controllers and source valve controllers. The accuracy in timing enabled by this setup is highly advantageous for the growth of

graded layers, superlattices, and digital alloys. Coupled with data recording functionality, the Emeralt computer control system greatly enhances both the efficiency of operation and the growth capabilities afforded to the grower.

2.4 System Upgrade Process

As in any major MBE maintenance cycle, careful attention to cleanliness is central to the upgrade of the ASU system. This is vital for maximizing the ability to maintain UHV chamber conditions and to minimize potential material contaminants. Converting one of the system's two chambers from III-V growth to II-VI growth significantly increases the difficulty in achieving this. The dual chamber upgrade process and the many additional considerations necessary for the conversion are discussed in the following.

2.4.1 *Preparation for System Cleaning*

The MBE upgrade commenced with the preparation of sources for venting. Heater temperatures were ramped down slowly to protect the pBN and graphite crucibles from potential damage due to thermal coefficient of expansion differences with source materials.

Prior to opening the chamber, a vent-pump procedure was used as a safety precaution against hazardous reactions of deposited materials with atmospheric gases. In particular, the pyrophoric characteristic of the P_4 allotrope of phosphorous can result in fire and dangerous explosions if exposed to quickly to oxygen. Similarly, arsenic reacts with the hydrogen present in air to produce arsine, a highly toxic gas [**26**]. The procedure involves repeatedly exposing the

chamber to atmospheric gases and then using the turbo pumping station to clear out resulting hazardous gases. By removing sudden exposure to full atmospheric conditions, the aforementioned dangers are minimized.

The full vent then follows and deposited materials are allowed to further oxidize until arsine readings decrease to safe levels. Components of the MBE were then removed and all ports were blank flanged except for one to allow for continued arsine monitoring. Parts were wrapped in UHV compatible aluminum foil for storage. While many were reused on the chamber designated for continued III-V growth, the II-VI chamber primarily used new parts. This was done to minimize potential contamination by III-V materials that could result from imperfectly cleaned components.

2.4.2 *Chamber Cleaning*

Both growth chambers then underwent a mechanical cleaning procedure to remove deposited materials. A number of protocols were established to prevent exposure of research team members to hazardous chamber materials. These started with the specification of required personal protective equipment. A DuPont Tyvek coverall was worn by all working in the lab as a barrier from particles and chemicals. Also for this reason, particulate respirators and gloves were used. When cleaning the chamber, other ports were covered with UHV compatible aluminum foil and the arsine detector probe was placed near the entrance of the working port. The work area was evacuated if any readings exceeding the Occupational Safety and Health Administration recommended permissible exposure limit of 50 parts per billion were encountered [**27**].

The cleaning process started with simple scraping with isopropyl alcohol (IPA) cleaned screwdrivers and other similar implements. For safety, care was taken to avoid aggressive scraping that would expose a large amount of unoxidized pyrophoric material. Furthermore, during all mechanical cleaning steps, water was sprayed over the scraping area to minimize spread of particulates into the air. Upon removal of a majority of the deposited material, each chamber underwent further finishing steps. Since the deposited materials were of lesser concern for the chamber designated for III-V growth, a simpler sandpaper cleaning method was used. Low fiber producing cleanroom wipes were used in conjunction with IPA to remove particles and clean away organic materials.

The more stringent removal requirements of the II-VI chamber dictate full cleaning to the stainless steel walls. This was achieved through the use of a rotary tool equipped with a steel brush attachment and extensive sandpaper and steel wool scrubbing in hard to reach areas. As in the III-V chamber, an IPA wiping followed to aid in particulate removal. A 1:50 nitric acid to deionized water solution was used to passivate the freshly exposed stainless steel chamber walls and was followed by another IPA wiping.

2.4.3 *High Temperature II-VI Chamber Bake*

Bakes are used in high vacuum applications to outgas contaminants and maximize the vacuum level potential of a system. Increasing chamber temperature increases the equilibrium vapor pressure of any materials condensed onto the walls. This promotes higher rates of evaporation enabling faster removal from the chamber by the vacuum system. Very high temperatures are therefore desired but

limitations are usually incurred by the maximum operating points of chamber components.

It was important to remove as much of the remaining III-V contaminants as possible from the II-VI chamber. Therefore, an initial chamber bake with ports blank flanged was used to remove the temperature limitations due to component specifications. In order to accomplish this, the original baking setup of the dual chamber system had to be modified to facilitate the single chamber bake. This original setup consisted of a series of fiberglass insulation filled panels that assemble into a box around the entire system. The new setup required disconnecting the II-VI chamber from the transfer chamber and shifting its position to allow for a newly fabricated panel to be added, completing the enclosure.

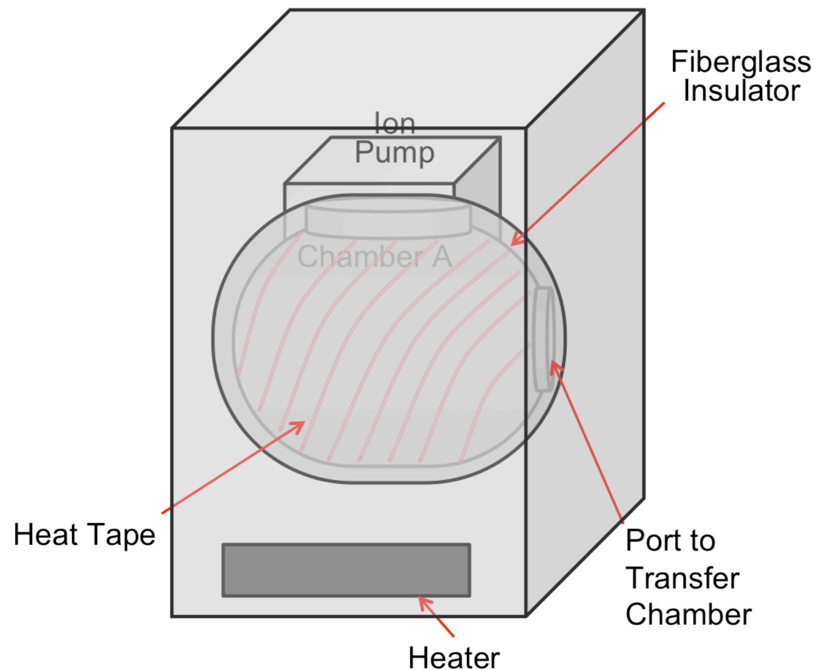

Figure 2.8: II-VI chamber high temperature baking setup (Courtesy: D. Ding)

The setup of the II-VI chamber bake is shown in Figure 2.8. The goal of the bake is to reach a chamber temperature of approximately 300 °C. However, the ion pump used during the bake must be maintained at a lower temperature. A heater is used to achieve a maximum of 200 °C in the baking box, an acceptable level for the ion pump. Heat tape wrapped directly around the chamber with an additional covering layer of fiberglass insulation enables the additional temperature difference desired for the chamber. This wrapping was done carefully to ensure highly uniform heating, necessary to undue stress on welds that could result in leaks.

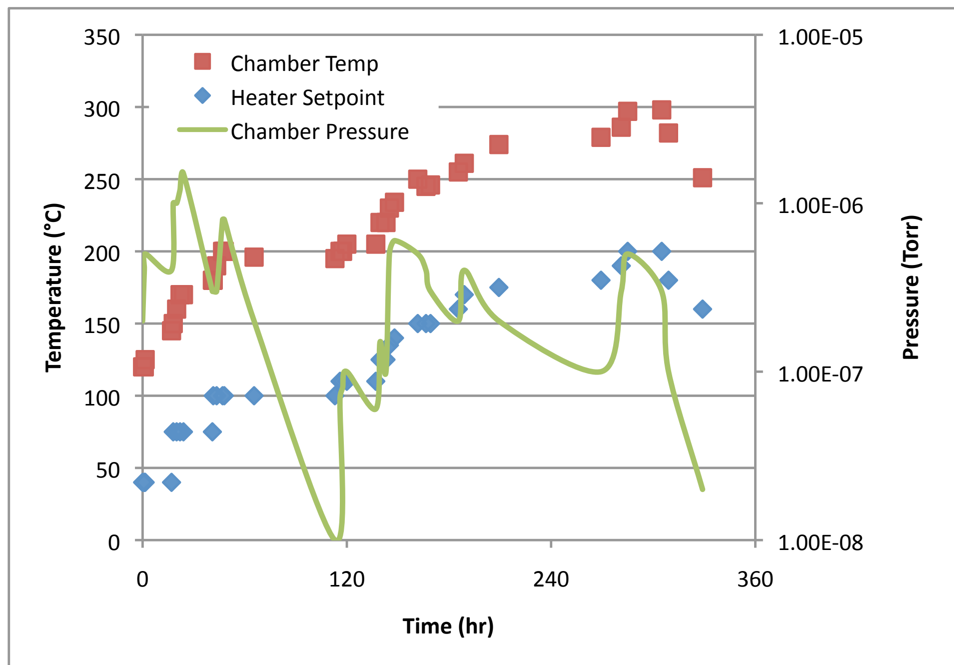

Figure 2.9: II-VI chamber pressure and temperatures versus baking time.

Thermocouple probes were placed in multiple locations on the chamber to monitor this uniformity. Heating tapes were individually controllable by variable duty cycle on-off controllers. The overall temperature ramp proceeded slowly to

ensure that uniform heating of each zone could be accomplished (Figure 2.9). The pressure was also monitored during this time. There is a general correspondence in pressure increases with faster ramps in temperature. This is explained by increases in evaporation rates and the amount of materials having reached their vapor points. At points where the temperature was held constant, the pressure lowers as evaporated materials are pumped out of the chamber. The entire bakeout was carried out over a period of 14 days and a maximum chamber temperature of 298 °C was recorded.

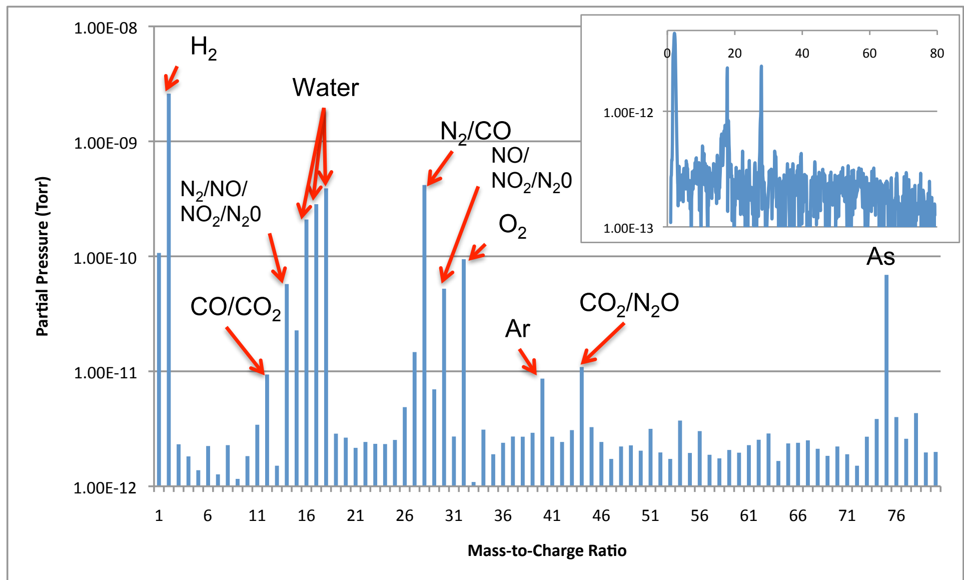

Figure 2.10: RGA partial pressure scans of the III-V chamber (main) and II-VI chamber post-bake (inset).

The success of the cleaning process is verified by comparing RGA output of the II-VI chamber with that of the III-V chamber (Figure 2.10). The most important observation is the lack of arsenic peak on the II-VI chamber reading, confirming significant reduction in semiconductor material via the cleaning

process. The peaks of the II-VI output are attributable to atmospheric contaminants such as water, nitrogen, and hydrogen. These are expected as the chamber was exposed to air to allow the addition of MBE components prior to taking the readings.

2.4.4 *Component Maintenance and Replacement*

In a typical MBE maintenance cycle, many components can be reused. However, as a measure to avoid III-V contamination, extensive cleaning or complete replacement was required for parts used in the II-VI chamber conversion. A selection of the MBE parts and their maintenance is now discussed with focus on achieving cleanliness and reliability.

The vacuum system for all chambers underwent major renovation to maximize reliability and longevity for the system. The ion pumps were disassembled. The pump bodies were sent out for chemical cleaning to remove all traces of III-V materials. Cathodic plates, used for gas capture, were fully replaced as were the anodic elements. High voltage feed-thrus were replaced due to their tendency to leak after extended use.

Cryopumps were also removed and sent out for rebuild. The high surface area carbon surfaces used to capture gases were replaced. This is especially vital for the II-VI chamber to prevent captured III-V materials from desorbing into the clean chamber. Necessary maintenance is also carried out on the mechanical parts of the helium compression system to promote future reliability.

On the III-V chamber, gate valves were cleaned and rebuilt. Again, to prevent potential contamination from incomplete cleaning, all new gate valves

were used on the II-VI chamber. Gate valves were oriented such that their sealing O-ring faces away from sources. This is to prevent particles from embedding into the rings, potentially causing leaks.

Heated windows are used on some ports to enable optical measurements throughout extended growth cycles. By applying the same principles used in chamber bakeouts, minimal material condensation occurs on the windows when kept at an elevated temperature. On the III-V chamber structural parts were cleaned and the tungsten heating filaments were replaced as they were nearing their expected lifetime. All new windows were used on the II-VI chamber.

Both manipulators underwent extensive maintenance. Due to cost and availability, full replacement was not an option. Instead, it was disassembled into many small parts that were either replaced or underwent careful mechanical and chemical cleaning. In an effort to further reduce risks of contaminating the II-VI chamber, the manipulator was reassembled and attached to an external chamber to outgas using its heater prior to final installation.

The final requirement for having all chamber components ready for growth was to prepare the substrate holders. Brand new holders were given a simple IPA rinse. Previously used holders required etching to remove deposited material. A concentrated nitric acid etch was used as it selectively etches III-V semiconductors versus the molybdenum in the substrate holder [**28**]. Before growth, all holders were outgassed in the high temperature stage of the prep chamber with completion verified using the RGA.

2.4.5 *Full System Bake*

After all in-vacuum components of the dual chamber MBE system were installed, the system was pumped down and checked for leaks. Upon completion of this, all unbakeable exterior components were removed, cooling water lines were purged using pressurized air, and the full system baking box was assembled. The liquid nitrogen supply lines were then connected to the cold trap. The baking box heaters were then ramped up at a rate of 1 °C/hr to a maximum of 200 °C. This temperature was maintained for 130 hours prior to a ramp down over a period of approximately four days. During all stages, the system vacuum was monitored and the partial pressures at the cold trap were recorded.

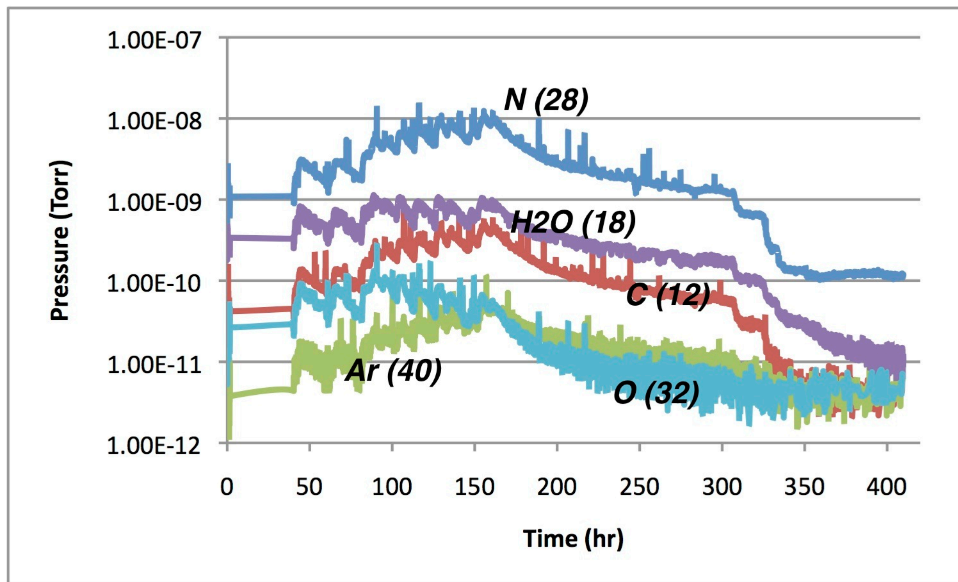

Figure 2.11: Partial pressures versus time recorded at cold trap during bake.

Prior to the bake, the II-VI chamber had a total pressure in the mid 10^{-9} Torr range. During the baking temperature ramp, the total pressure increased as is also reflected in the recorded partial pressures (Figure 2.11). As in the initial II-VI

chamber bake, this is due to the increased evaporation rates of materials condensed on chamber walls. At the point where the ramp up completed (approximately 170 hours), the partial pressures began to decrease as pumping rates overcame the evaporation rates. At approximately 330 hours, the baking temperature ramp down began. Partial pressures correspondingly decreased as their evaporation rates also decreased with temperature. When room temperature was reached, the II-VI chamber total pressure was 3×10^{-10} Torr. This lower reading suggests that chamber contaminants had been reduced as the pumps have less outgassing to overcome.

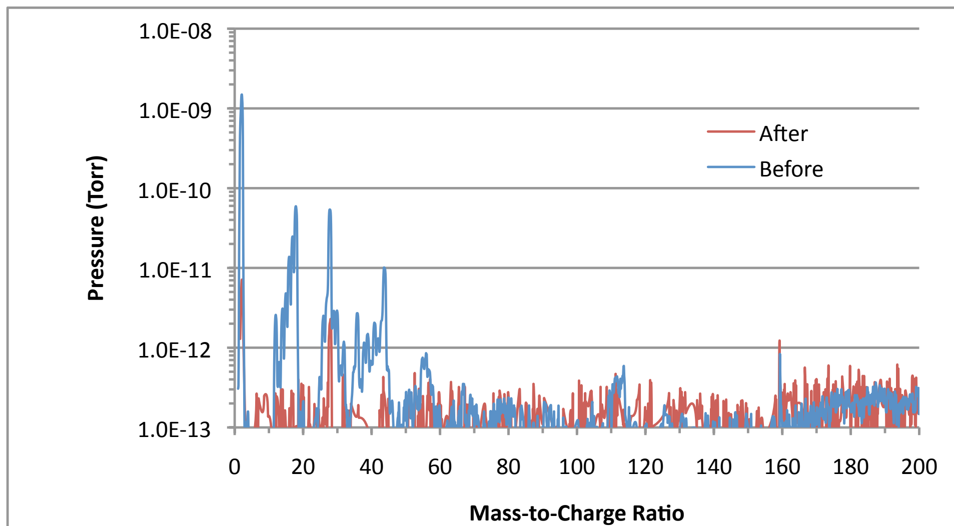

Figure 2.12: Analog RGA scans at the cold trap before and after bake.

Further confirming this is a comparison of the RGA analog scan output immediately before and after the bake (Figure 2.12). In this, hydrogen (m/z = 2) and water (m/z = 16,17,18) is reduced by over 2 orders of magnitude. Similarly, nitrogen (m/z = 28) and carbon dioxide (m/z = 44) are reduced by over an order of magnitude, as are many other atmospheric gases.

The scan also demonstrates the success of measures taken to minimize outgassing of II-VI materials. The cadmium partial pressure (m/z = 56,112) is reduced while selenium (m/z = 160) exhibited a negligible rise in partial pressure. No other significant peaks corresponding to other II-VI semiconductors is noted.

3 GROWTH CALIBRATION FOR II-VI SEMICONDUCTORS

3.1 Growth Preparation

3.1.1 *Substrate Mounting*

Substrate temperature control plays a vital role in nearly all stages of MBE growth as it dictates processes occurring at the wafer surface. Since the ASU 6.1 Å II-VI and III-V dual chamber MBE system utilizes an indirect thermocouple measurement for control, it is important to understand the relative heating characteristics of the substrate holders used. The types of wafer holders used and their heating characteristics are discussed in the following.

In the ASU system, wafer holders facilitate substrate heating via two general methods, direct and indirect. The former holds the wafer such that heater radiation is absorbed within the actual sample and is also known as In-free mounting. Conversely, the substrate holder or a carrier wafer absorbs the radiant heat in the latter which is then transferred by primarily conductive means to a substrate mounted to its surface.

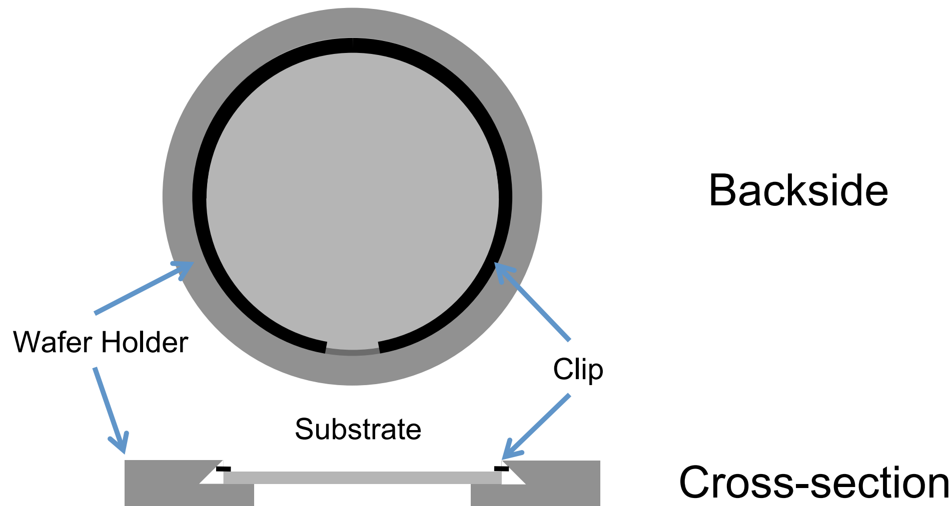

Figure 3.1: Schematic of a full-wafer holder.

During the system calibration, direct heating was accomplished by placing a wafer into an open molybdenum frame. Full wafer holders of this kind used a circular ceramic clip to hold the wafer securely onto the frame (Figure 3.1). New quarter wafer holders were also designed that use three small clips secured by screws to hold the substrate.

The indirect wafer heating method used involved adhering the substrate to a Si carrier wafer using In solder. This method has a number of drawbacks for device quality growth. The foremost of these is that In can unintentionally get incorporated as a dopant for II-VI materials or as a constituent for III-V materials. It also presents a number of practical issues. Applying the In to the mount requires time and care. Removing residual In from the sample backside after growth is also challenging. As a result, the In-free mounting methods are highly preferred for achieving high quality devices and materials.

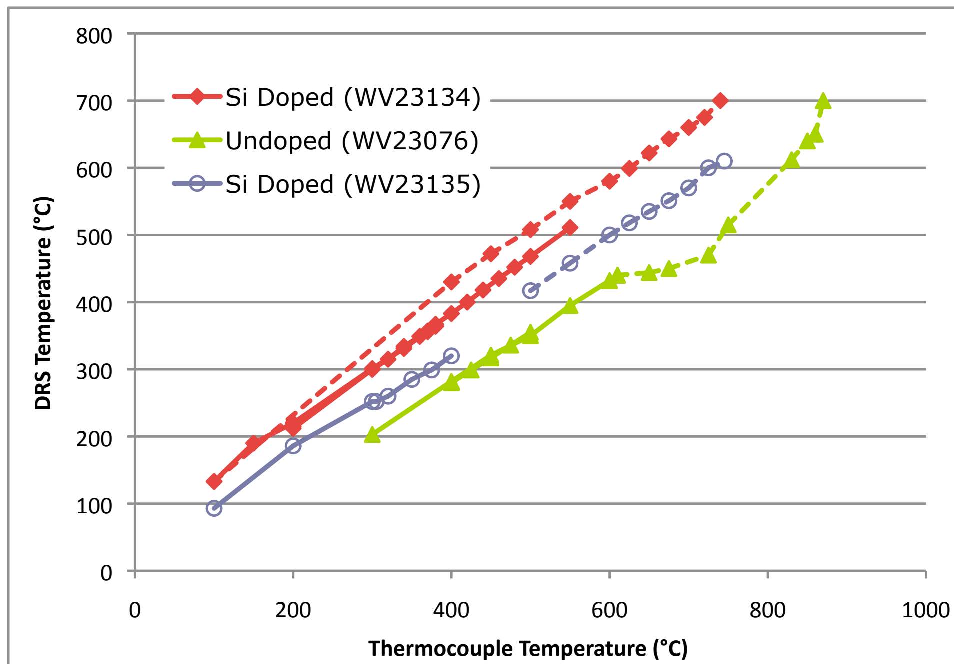

Figure 3.2: DRS temperature vs. thermocouple temperature for substrates of different lots mounted with In-free wafer holders under equilibrium (solid line segments) and fast positive ramp (solid line segments).

In early calibration runs, a high amount of temperature variability was observed between different substrates and substrate holders. Therefore, an investigation of substrate calibration data was carried out. Full equilibrium calibrations were taken by waiting for temperatures to stabilize at each recorded point. Observations were also recorded during fast ramps, over 50 °C/min, such as those used during deoxidation procedures. The data revealed that wafer lots have a significant effect on the heating characteristics (Figure 3.2). This is due to varying amounts of infrared heater absorption and emission within the substrates. Doping level was shown to be a major factor. This is reflected by the lowest DRS temperatures relative to the thermocouple reading being attained for the undoped

substrate corresponding to a lower amount of infrared absorbing free carriers. However, similarly doped subtrates still exhibited a high level of variability as well. This is likely due to a combination of other substrate properties including carrier mobility, thickness, and resistivity.

The absorption rate of each substrate displayed a clear effect on the temperature characteristics under ramp up as well. On the more highly absorbing substrates, the transient curve exceeded the equilibrium curve. Conversely, on the low absorbing undoped substrate, the transient curve was lower in temperature relative to the equilibrium curve. Knowing these characteristics is vital for achieving successful deoxidation.

Due to the noted variability, it is clear that substrate calibrations are required for directly heated substrates. Fortunately, variation within wafer lots was far less significant, typically less than 5 °C. This suggests that a single calibration is applicable for each wafer lot.

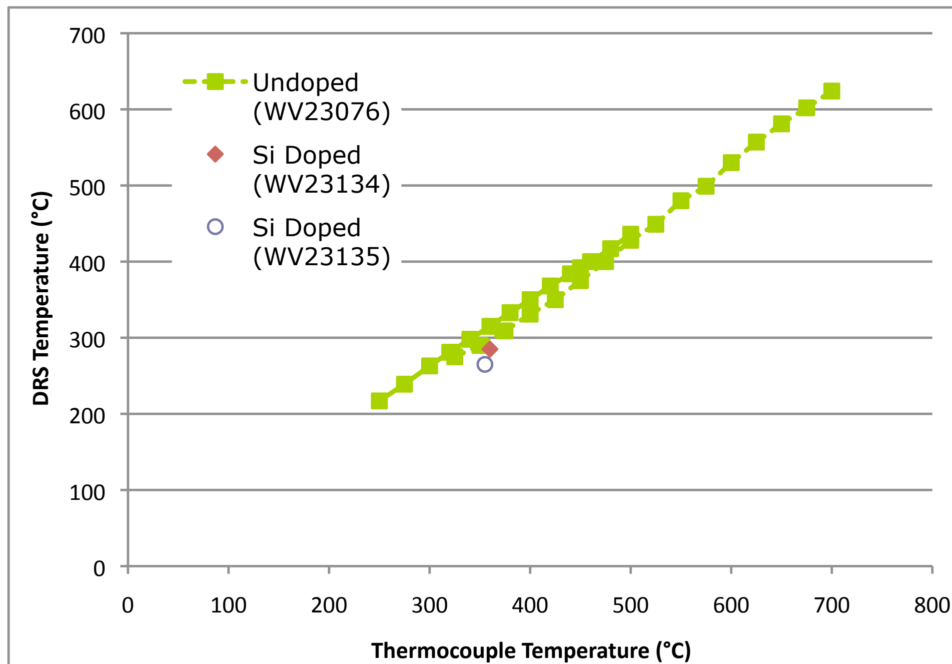

Figure 3.3 DRS temperature versus thermocouple temperature for substrates of different lots using In mounting.

By using the Si carrier wafer to absorb the heater radiation, the variation between wafer lots is effectively removed. This is confirmed in the obtained data as the same wafer lots display a significantly reduced spread (Figure 3.3). The variation that is noted is attributed to differences in mounting technique between samples. The data also displays transient temperatures closer to the equilibrium curve.

This study suggests that In-mounting reduces substrate temperature calibration requirements. For this reason, In-mounting was used for a majority of the II-VI system calibration. However, the more stringent contaminant avoidance requirements of materials studies and device production dictate future use of the

direct holders. The discussed investigation points to the importance of obtaining a temperature calibration curve for each wafer lot used.

3.1.2 *As-Free GaAs Substrate Deoxidation*

GaAs (001) substrates were selected for a majority of the calibration runs in order to reduce costs relative to the ZnTe or GaSb substrates planned for use in 6.1 Å II-VI and III-V integrated devices. Typically, GaAs substrates are deoxidized under an As flux to prevent desorption during substrate heating. Due to contamination concerns, this is not allowable in the II-VI chamber. As a result, excessive heating must be avoided to prevent severe degradation of the surface prior to growth.

Bousquet et al. suggest heating until a (2×1) RHEED pattern is observed when using an epi-ready GaAs (100) substrate [**29**]. In their work, this pattern occurs between 580 °C and 600 °C and is accompanied by an increase in brightness indicating the desorption of the oxide layer. Similarly, Cornelissen et al. [**30**] reported streaky RHEED at 580 °C. Hence, the initial procedure used for deoxidation during the II-VI chamber calibration was to heat until a (2×1) pattern was observed.

A ramp to fail test was carried out to observe the evolution of RHEED during oxidation. At that time, the pyrometer was used for substrate temperature measurements. During measurements, the heated window was turned off to avoid inaccurate readings caused by stray radiation from the filaments. During the ramp, (2×1) RHEED was observed at 700 °C on the thermocouple and 570 °C on the pyrometer. At 800 °C/658 °C (thermocouple/pyrometer), the RHEED evolved to

a (4×1) pattern. Further heating resulted in the appearance of spottiness characterized by a chevron shape concluding with the appearance of 3D rings at 905 °C/750 °C (thermocouple/pyrometer). This suggested that the deoxidation process was fairly forgiving of the maximum temperature.

As growths were carried out, however, inconsistent observations were noted. The appearance of a (2×1) reconstruction did not always happen prior to reaching very high temperatures. In other cases, the RHEED turned spotty before this reconstruction appeared. This is a sign of a 3D surface caused by excessive As desorption. The most successful desorptions involved ramping down the temperature after an increase in intensity and observation of (2×1). Many of these were carried out using In-mounted substrates suggesting deoxidation issues may have been linked with poor temperature calibration.

In order to establish a consistent routine, a deoxidation study was carried out with careful attention to reconstruction observations relative to substrate temperature measured via DRS. A slow ramp rate of 10 °C/min was used from 540 °C (DRS) to observe the RHEED evolution. During this time brightness of the specular spot was objectively measured using the RHEED oscillation feature of the software. As the ramp continued through the mid-500 °C range, the weak GaAs reconstruction started to become streakier. A significant increase in brightness occurred at 585 °C signaling significant desorption of the oxide layer. Weak second order lines began to appear at 605 °C and strengthened with continued ramping suggesting As had started to become deficient at the surface. Beyond 625 °C, the RHEED pattern began to darken meanwhile the streakiness

continued to improve until 640 °C. Beyond this point, the pattern degraded and the substrate surface began to appear hazy. The darkening and pattern degradation are consistent with a decrease in order on the substrate, suggesting a poor surface for growth initiation.

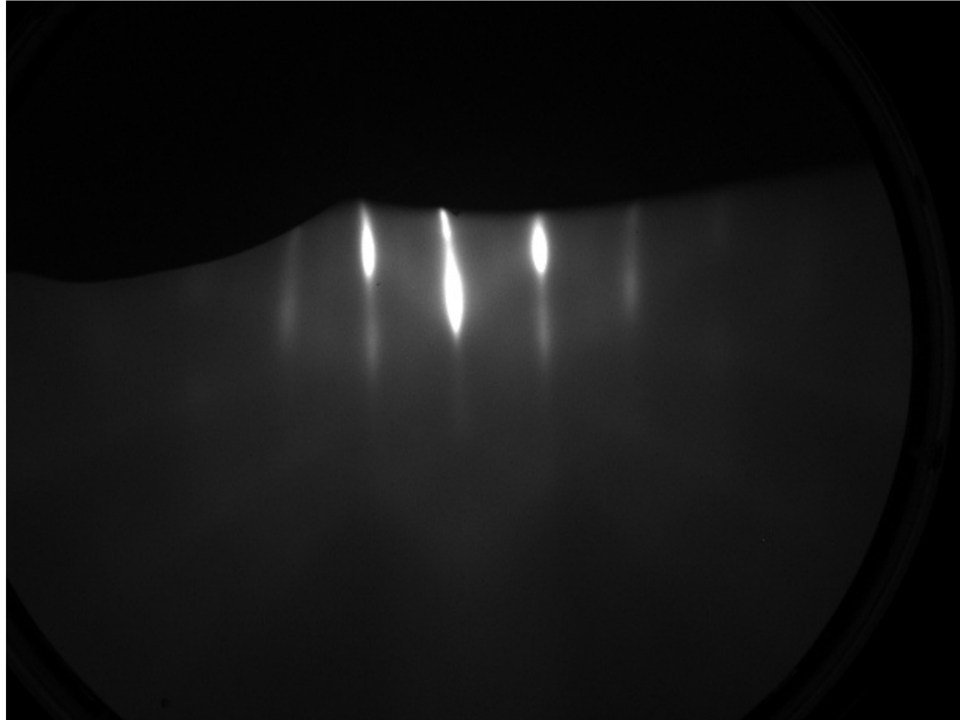

Figure 3.4: (2×1) RHEED pattern of GaAs (001) substrate at a peak deoxidation temperature of 620 °C (DRS).

Based on this information, a procedure of quickly ramping the substrate quickly past RHEED brightening to temperature of 615 °C followed by a 1 min to 2 minute hold time was adopted. This extra hold time is used to ensure complete oxide desorption. During the hold, the RHEED is closely monitored and the substrate temperature dropped if the pattern begins to get spotty or darken to prevent further surface degradation. Using this procedure, (2×1) patterns such as

that shown in Figure 3.4 were consistently attained and streakier RHEED was maintained during ramp down and after Zn flux initiation. Runs experiencing brief substrate temperature overshoot to temperatures around 630 °C to 640 °C were notably streakier. Further experimentation is required to confirm the reliability of this observation and warrant implementing it into the deoxidation process.

3.2 Source Flux Calibration

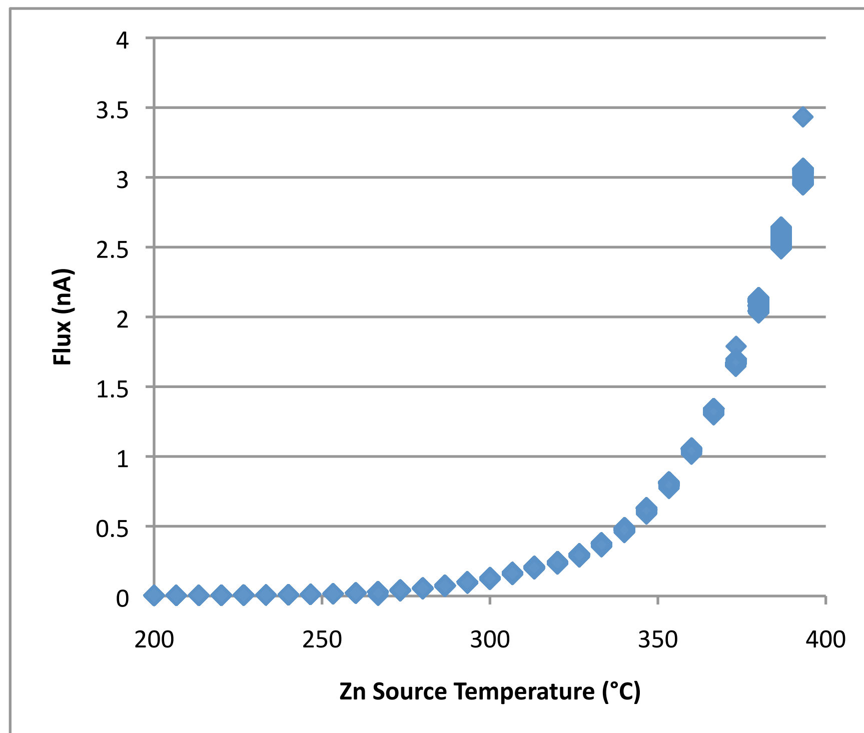

Figure 3.5: Zn flux versus source temperature.

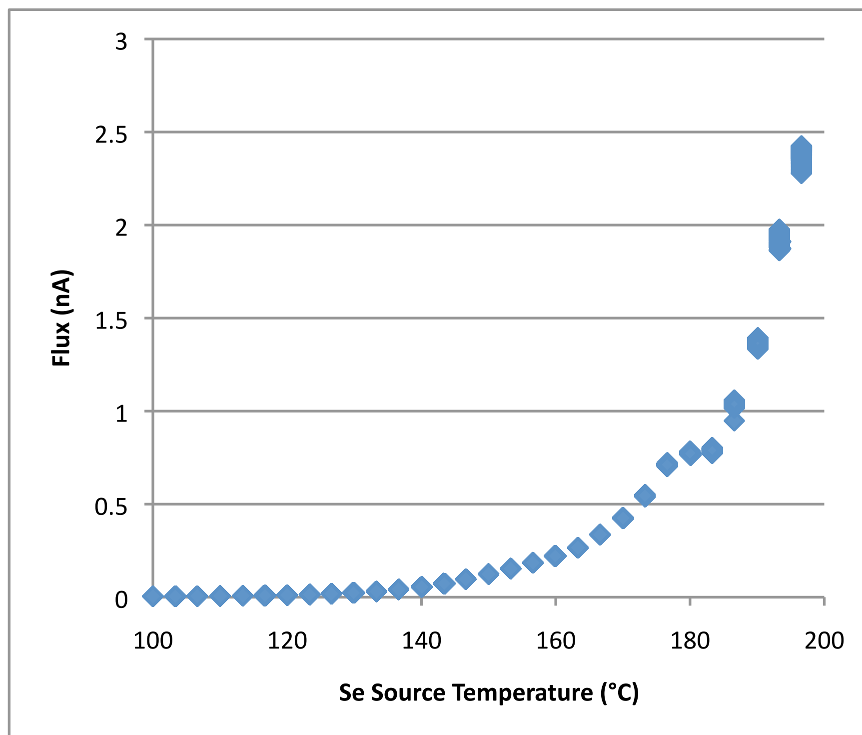

Figure 3.6: Se flux versus source temperature.

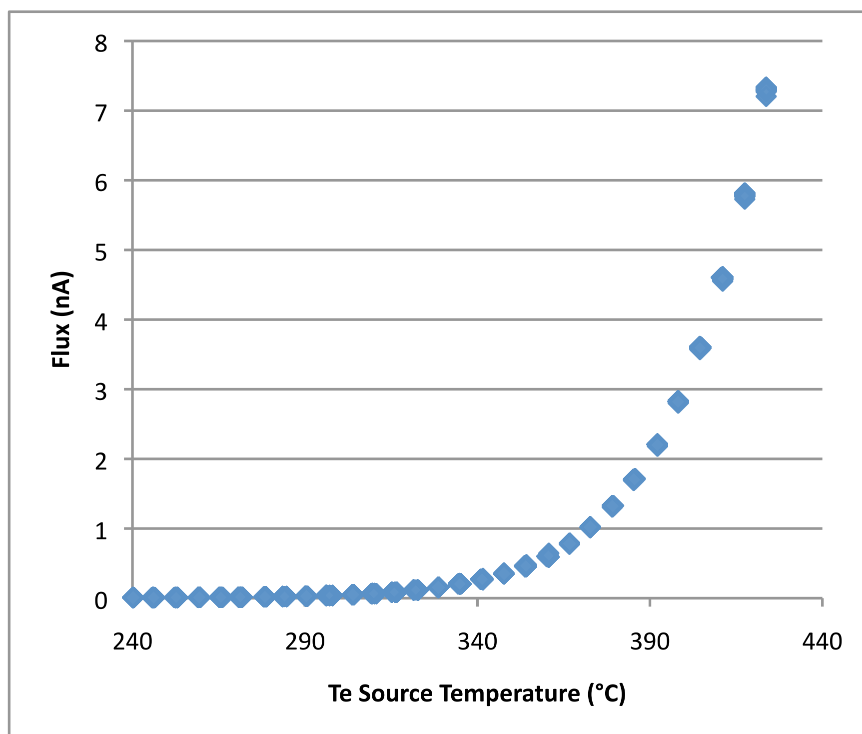

Figure 3.7: Te flux versus source temperature.

In order to calibrate growth conditions, knowledge of the source heating characteristics and flux characteristics are needed. Stable source flux output is best achieved by slowly ramping to the desired growth temperature. This is to ensure uniform heating of the material. Flux versus temperature curves were obtained for Zn (Figure 3.5), Se (Figure 3.6), and Te (Figure 3.7) by using a slow ramp, allowing over 10 minutes for stabilization and then averaging flux readings over 1.5 minutes. Overall, these curves exhibit the expected exponential shape and enable determination of source temperatures to achieve desired growth conditions. Since some drift can occur over time, fluxes were checked periodically to maintain consistent flux ratios.

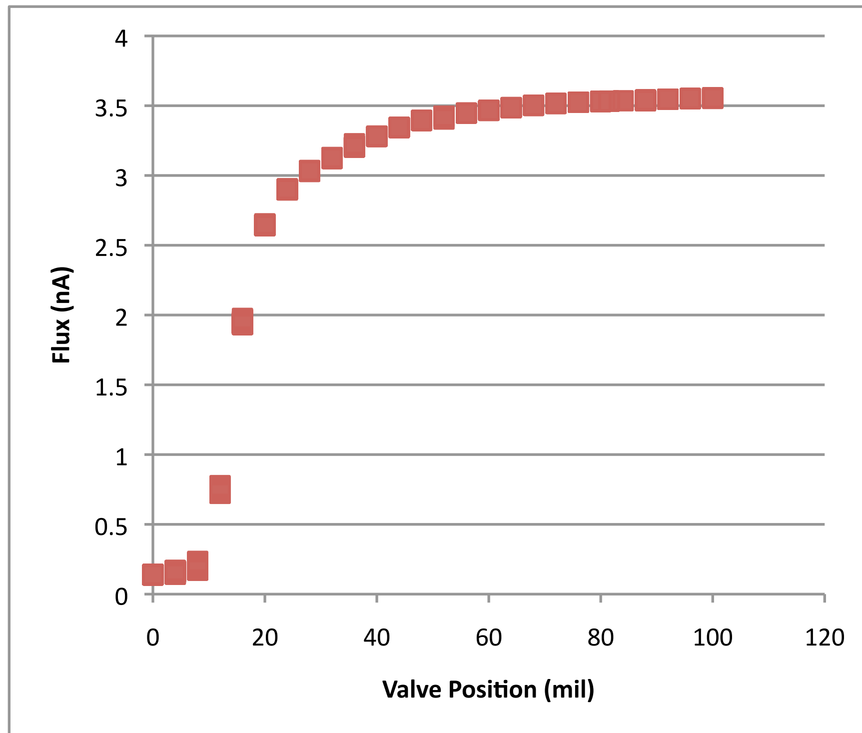

Figure 3.8: Se flux versus valve position for Se cell bulk temperature of 200 °C.

The Se valve enables quick flux adjustment. Its characteristic displays a high slope in the lower range and eventually saturates as it approaches the fully open value (Figure 3.8). This high slope exacerbates inaccuracies caused by any drift in flux over time therefore frequent calibrations are needed for any growths using this zone. Also of note, the low values below a valve position of 8 mil were removed by a later recalibration of the valve positioning system. The calibration process also revealed excess flux for approximately 5 minutes following initial opening. Therefore, a procedure was implemented where the valve is opened with shutter closed for at least ten minutes prior to initiating growth.

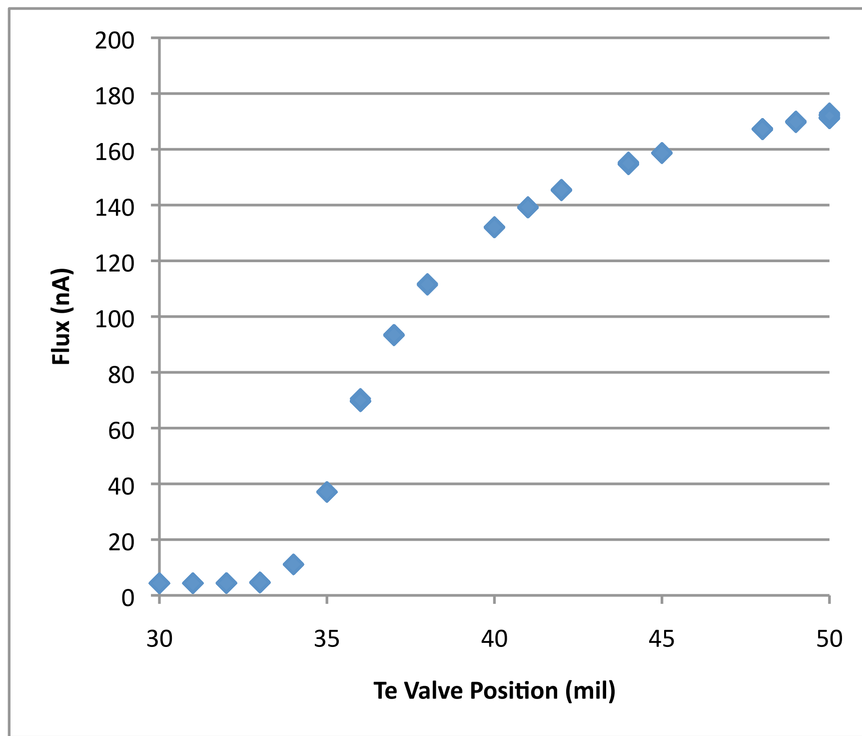

Figure 3.9: Te flux versus valve position

A similar characteristic is noted for the Te valve (Figure 3.9). As with the Se valve, a high initial slope followed by a slow approach to the fully open level

is noted. Again, this requires frequent calibration to ensure accuracy of these fluxes. Unlike the Se valve, this source does not demonstrate an initial flux burst after opening. Therefore, no waiting time after initial valve opening is required prior to use.

3.3 ZnSe Growth Calibration

With the flux characteristics of the sources determined, experimentation to find optimum growth procedures and parameters could begin. The first step is to establish a ramp down procedure from the deoxidation temperature. The As-free deoxidation procedure results in a Ga terminated surface that has a tendency to form compounds with group-VI elements that can hinder proper growth [**31**]. In order to avoid this, all growths were initiated using a Zn flux starting 100 °C over growth temperature during ramp down. At this point, RHEED typically remained unchanged from its streaky/spotty reconstruction.

The next step was to determine the source operating conditions. For ZnSe, the desired flux ratio achieves stoichiometric conditions at the substrate surface [**32**]. Since the flux gauge sensitivity varies by constituent as does sticking coefficient, the measured flux ratio for this condition is not necessarily 1:1. Fortunately, RHEED reconstructions are often dependent on the constituent ratio at the surface. Previous reports [**30**,**32**] have noted that Zn rich surfaces are associated with a c(2×2) pattern and Se rich surfaces display a (2×1) pattern. Under stoichiometric conditions, these reconstructions are superimposed with weaker second order lines.

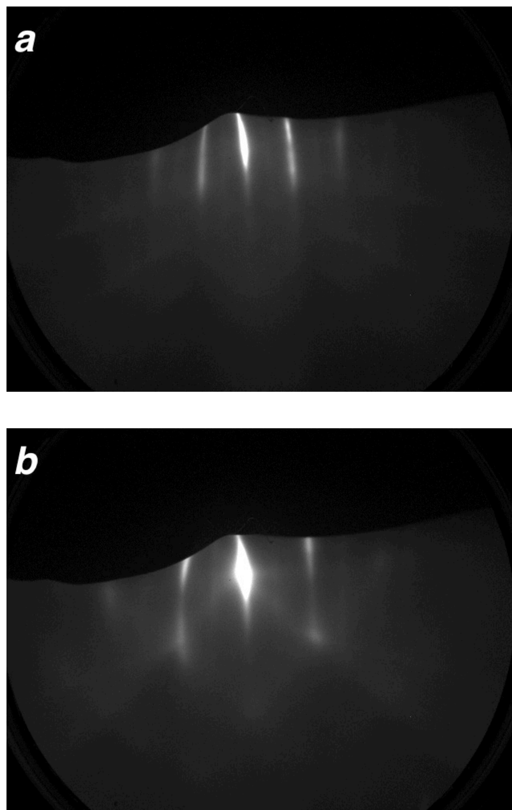

Figure 3.10: RHEED reconstructions for (a) [110] azimuth and for (b) [100] azimuth near the stoichiometric condition.

The II-VI observations were consistent with those reported in literature. In order to assure either Zn rich or Se rich surfaces, the opposite shutter was temporarily closed during growth. In both cases, stronger second order lines appeared in their respective reconstruction. By adjusting the source temperatures and Se valve position, the optimal near-stoichiometric growth zone could be located (Figure 3.10). During initial growths, this transition zone appeared for measured flux ratios (J_{se}/J_{Zn}) between 2 and 3 therefore values in this range were used for all calibration experiments.

Achieving an ideal combination of flux ratio and substrate temperature enable surface processes that promote high quality, uniform crystal growth. Using the experimentally determined ideal flux ratio range above, samples were grown over a range of substrate temperatures. The ZnSe films range in thickness between 1.25 μm and 6.40 μm. Growth rates were independent of substrate temperature within the tested range. Values between 0.21 μm/hr and 0.26 μm/hr were obtained for the initial growths. In order to achieve higher growth rate, overall flux was increased with resulting samples attaining rates between 0.52 μm/hr and 0.59 μm/hr.

The quality of these crystals was assessed using the full width half maximum (FWHM) of X-ray diffraction (XRD) ω-2θ rocking curves (Figure 3.11). This technique measures the intensity of diffraction peaks over a range of angles. The peak diffraction angle is dependent on lattice constant. Variation of lattice constant appears as a broadened peak that is the summation of individual diffraction peaks within the material. This variation is highly correlated to the amount of structural defects within a material and hence is a good indicator of quality.

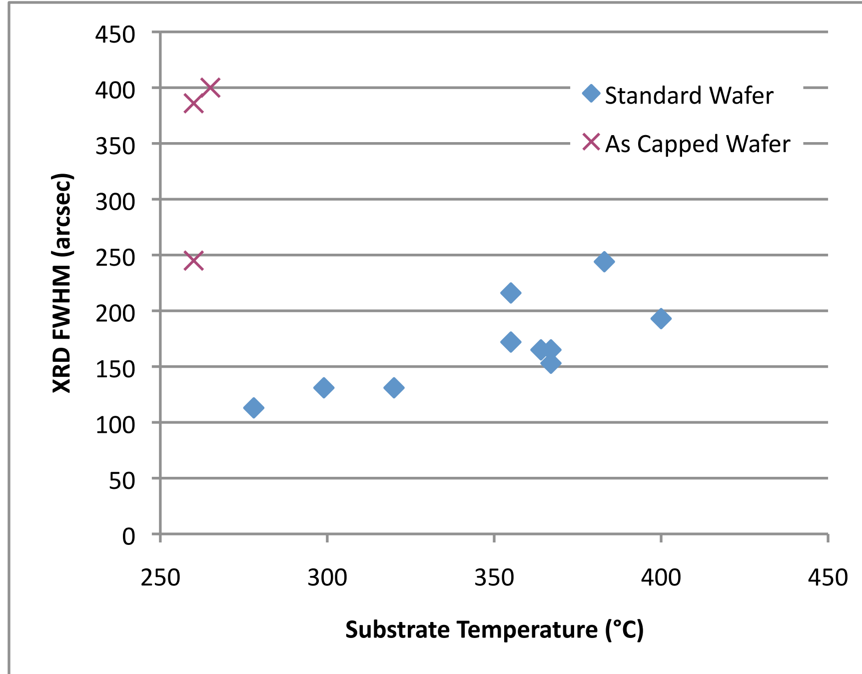

Figure 3.11: XRD ω-2θ FWHM versus substrate temperature of ZnSe samples grown using standard deoxidation procedure and low temperature As cap desorption.

The ZnSe XRD FWHM results are in the range of published values for ZnSe grown on GaAs (001) substrates [**33**,**34**,**35**]. An increase in ZnSe crystal quality with decreasing substrate temperature is observed for samples that employed high temperature deoxidation procedures. Since other growth procedures and conditions were varied between these samples, the data was analyzed to ensure the trend was not due to other factors. Thickness, in particular, has a direct theoretical relation to the XRD line width [**36**]. However, there is no significant correlation between sample thickness and the measured FWHM suggesting that this effect is negligible compared to that of temperature.

It is unlikely that the samples grown using low temperature As cap desorption signal a boundary to the aforementioned trend. Rather, this points to the need for further development of this process. Potential causes for the higher line width of these samples include incomplete desorption of the amorphous As layer and a poor GaAs buffer layer.

The FWHM values attained during the calibration support that the system upgrade was successful in fostering quality growth through contaminant minimization. The data suggests lower temperatures would further improve the material quality. A deeper investigation into the effect of flux ratio may also be informative. This could include both a wider range of flux ratios and a sensitivity check near the stoichiometric ratio. The latter is of interest due to the best sample having implemented a valve adjustment procedure that was used to achieve the optimal RHEED from Figure 3.4.

3.4 ZnTe Calibration

3.4.1 *Growth Condition Experimentation*

As with ZnSe, the ZnTe growth uses an initial Zn flux to prevent the formation of III-VI compounds at the interface. This is started 100 °C above the desired growth temperature during ramp down. At this time, there was typically either no change or a slight increase in spottiness of the RHEED pattern.

During initial growths, Zn and Te shutters were alternately closed in order to observe the resulting RHEED reconstructions. In the Te-rich case, a (2×1) reconstruction with strong second order lines was noted. Conversely, a c(2×2)

reconstruction corresponded to a Zn stabilized surface. These observations are consistent with those recorded in literature [**36**,**18**,**37**,**38**].

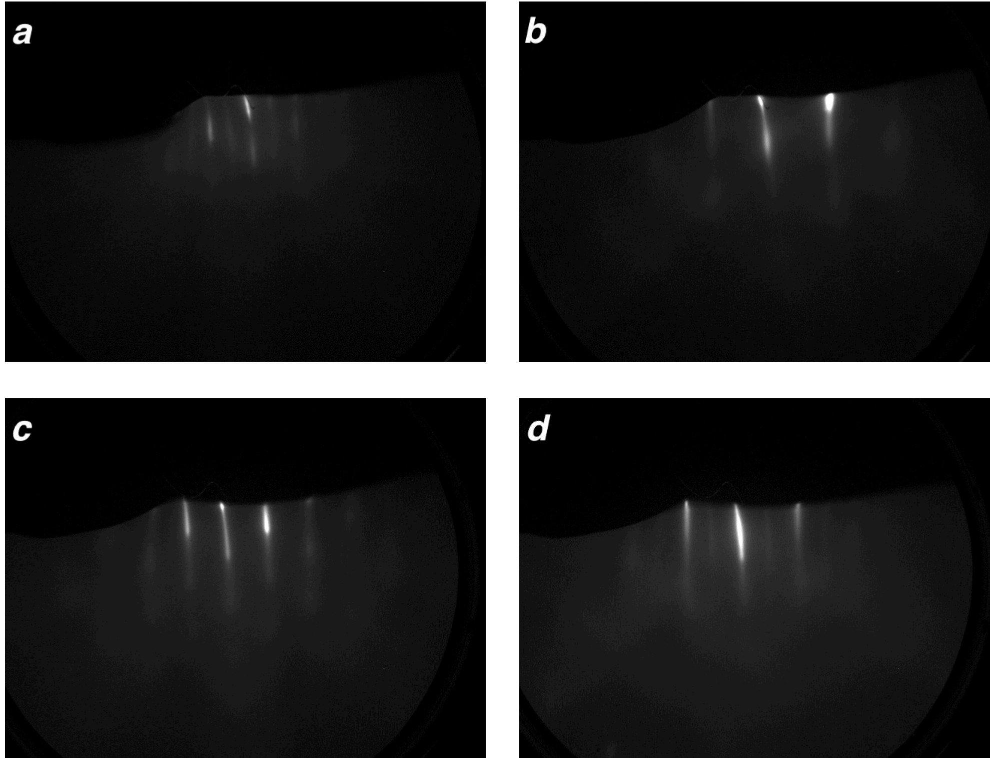

Figure 3.12: RHEED images for Te to Zn ratios of 1.46:1 (a, b) and 1.26:1 (c, d) in [110] azimuth (a, c) and [100] azimuth (b, d).

The focus of the initial growth condition experimentation was to locate an optimal substrate temperature range. Measured Te to Zn flux ratios between 1.25:1 and 1.5:1 were used for a majority of samples grown for this purpose. This was selected as a middle value of the wide range of ratios cited in literature for achieving successful growths [**18**,**37**,**39**]. These ratios appear to be in the transition zone of the RHEED. While not entirely consistent, samples with a higher Te:Zn ratio tended to have a (2×1) reconstruction whereas those with a

lower ratio more often had a c(2×2) reconstruction (Figure 3.12). This suggests that these ratios may be near the stoichiometric point.

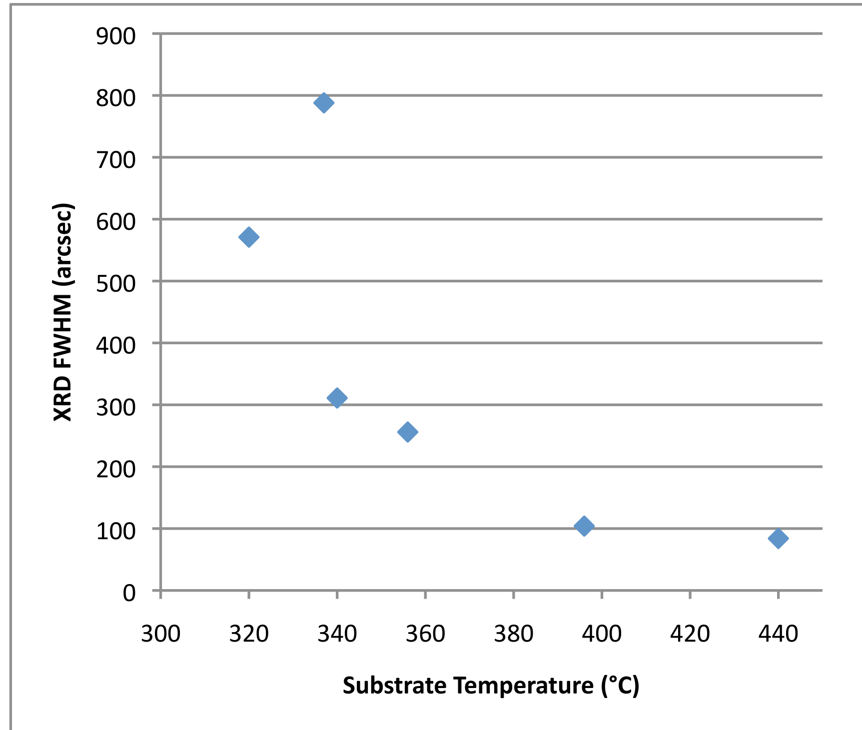

Figure 3.13: XRD ω-2θ FWHM versus substrate temperature for ZnTe samples.

The XRD ω-2θ rocking curves show a trend of decreasing FWHM values as the substrate temperature is increased (Figure 3.13). This signifies an increase in the structural quality of the ZnTe epilayers at the upper temperature range of the grown samples. A potential explanation for this is that the additional thermal energy provided to the substrate helps adatoms reach thermodynamically stable sites in the crystal [**38**]. This would be especially critical as the lattice relaxes from the strain induced by the 7.9% mismatch with the GaAs substrate. It is unlikely, however, that this trend would continue significantly beyond the range

of the grown samples due to reported faceting resulting from high desorption rates above 450 °C [**36**].

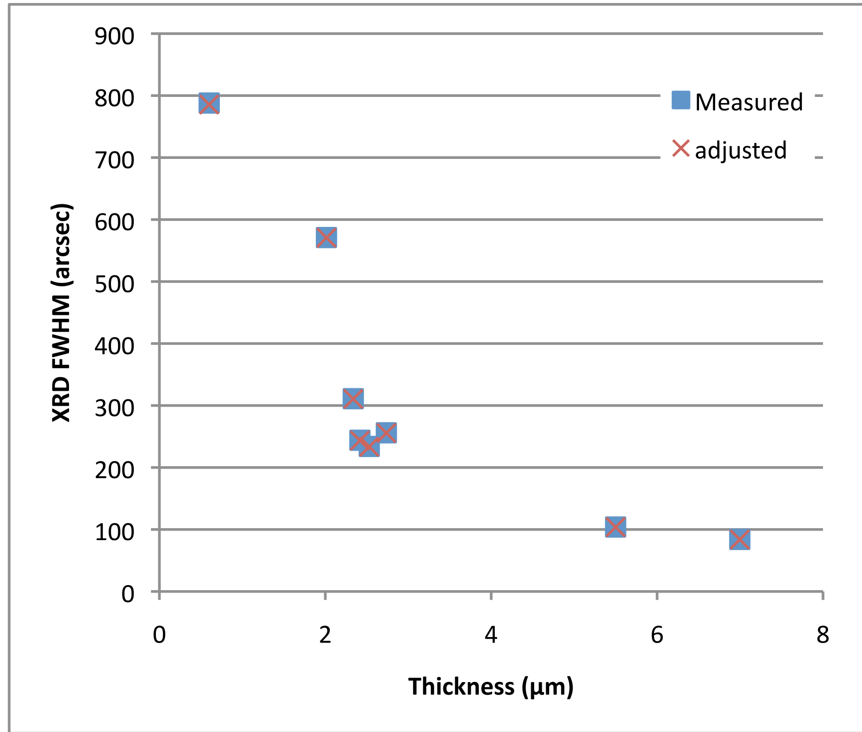

Figure 3.14: Measured XRD ω-2θ FWHM and thickness broadening adjusted FWHM versus thickness of ZnTe samples.

In order to verify that substrate temperature is the dominant factor in the trend observed in Figure 3.13, other relations are examined. The first of these is XRD ω-2θ FWHM versus epilayer thickness (Figure 3.14). As mentioned in the ZnSe section, crystals incur thickness dependent linewidth broadening, β_L [**36**]. This is described by:

$$\beta_L^2 = [4\ln 2/(\pi h^2)](\lambda^2/\cos^2\theta)$$

where h is the layer thickness, λ is the beam wavelength, and θ is the Bragg angle. The overall measured broadening, β_M is calculated by:

$$\beta_m^2(hkl) = \beta_0^2(hkl) + \beta_d^2(hkl) + \beta_\alpha^2(hkl) + \beta_c^2(hkl) + \beta_r^2(hkl) + \beta_L^2(hkl)$$

which includes other broadening mechanisms [**40**]. These are used to calculate adjusted FWHM values with the thickness dependent linewidth broadening removed. It is clearly seen in Figure 3.14 that this has a minimal effect. This shows that the FWHM trend is most likely caused primarily by other factors which is consistent with temperature being dominant.

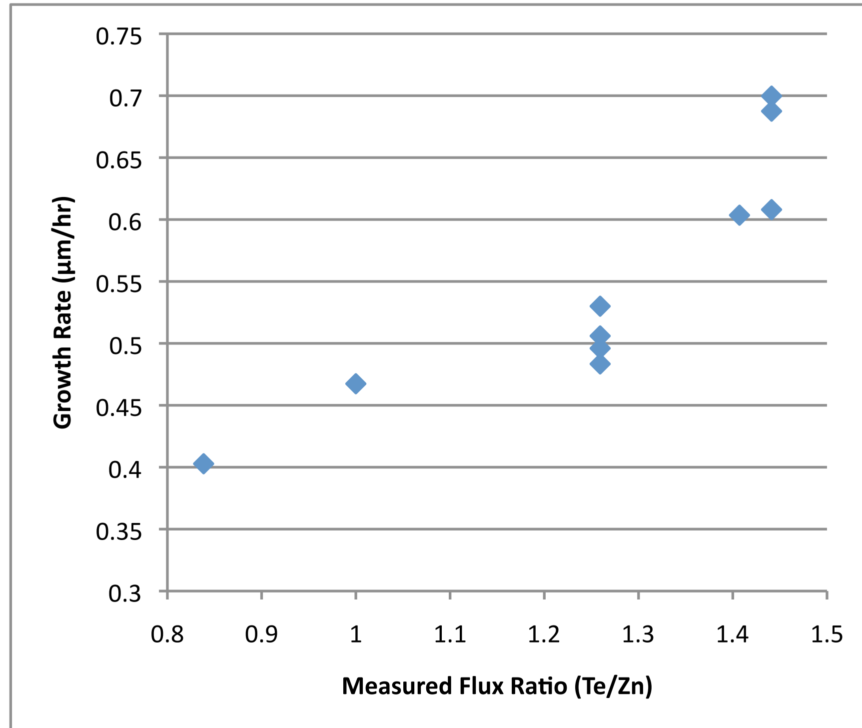

Figure 3.15: Growth rate versus measured flux ratio for ZnTe samples.

A strong positive trend between growth rate and temperature was noted within the data. Rather then being a direct effect, it is most likely that this is the result of the corresponding flux ratios (Figure 3.15). Within the range of flux ratios used, the growth rate increased with increasing Te content, evidence that these growths are within the Zn-rich regime. This further suggests that the

observations of both Zn-rich and Te-rich RHEED reconstructions may only signal that the measurements are near the crossover, not actually at it. In order to better understand this and other growth rate relations, a designed study was needed.

3.4.2 *RHEED Oscillation Growth Rate Study*

The investigation of ZnTe growth rate began by citing a number of factors that could be potentially influential. In order to effectively test all these, an efficient method to record the growth rate for different factor combinations without the need for individual growths was required. RHEED intensity oscillations are phenomena that are frequently used in MBE growth to obtain this in situ and have been previously reported for ZnTe[**41**]. These occur due to the diffuse scattering of the specular beam as partial layers are formed during two-dimensional layer-by-layer growth [**20**]. Since the oscillation period is directly related to the growth of an individual layer, the growth rate can be extracted.

A highly smooth and uniform surface is required in order to observe RHEED oscillations. The procedure used to achieve and maintain this during the study was developed using parameters from Najjar et al [**41**] as a starting point. It was as follows. An undoped GaAs substrate was deoxidized using the standard procedure. The Zn shutter was opened 100 °C above the growth temperature of 355 °C. After opening the Te shutter, the sample was grown under rotation for 25 minutes during which time RHEED became very streaky and displayed a c(2×2) reconstruction. At this point 20 migration enhanced epitaxy (MEE) cycles were utilized to smooth the surface. After a full growth interruption under a Te flux, oscillations were observed.

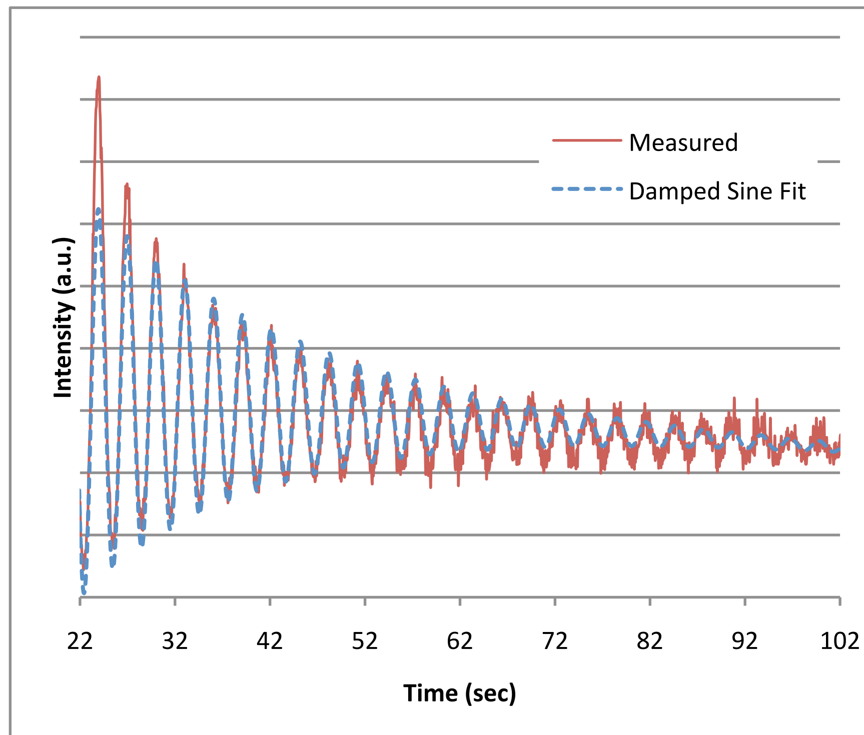

Figure 3.16: Example of RHEED oscillation obtained during ZnTe growth rate study with fitted damped sine wave.

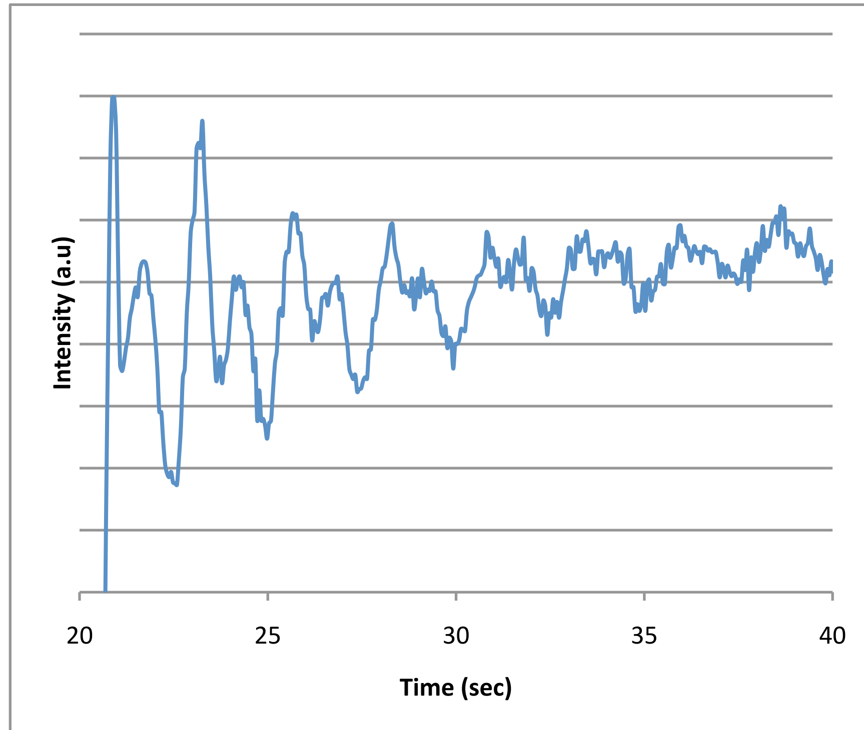

Figure 3.17: RHEED oscillation displaying double peak due to a misaligned electron beam.

The oscillations were tracked with Staib Instruments kSA400 software. Using this, it was determined that the strongest oscillations were recorded with the electron beam aligned to the [110] direction and interruption of the Zn source (Figure 3.16). Slight deviations from the [110] direction resulted in decreased signal-to-noise ratio and double peak behavior (Figure 3.17). After achieving quality oscillations, the growth rate was then extracted by fitting a damped sine wave to the measured waveform.

Throughout the measurement process, the quality and length of the oscillations would deteriorate. For most cases, a series of MEE cycles successfully restored the oscillations. In certain occasions, and more commonly at

low substrate temperatures, this did not help. At these times, an anneal at approximately 420 °C for 10 minutes was used to increase surface kinetics and return the 2-D growth surface.

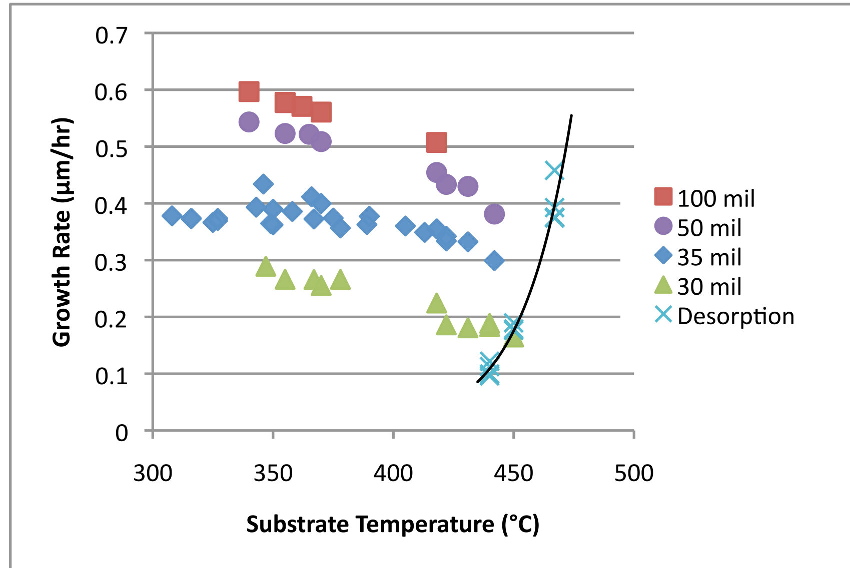

Figure 3.18: Growth rate versus substrate temperature for various Te valve. Desorption rate also shown.

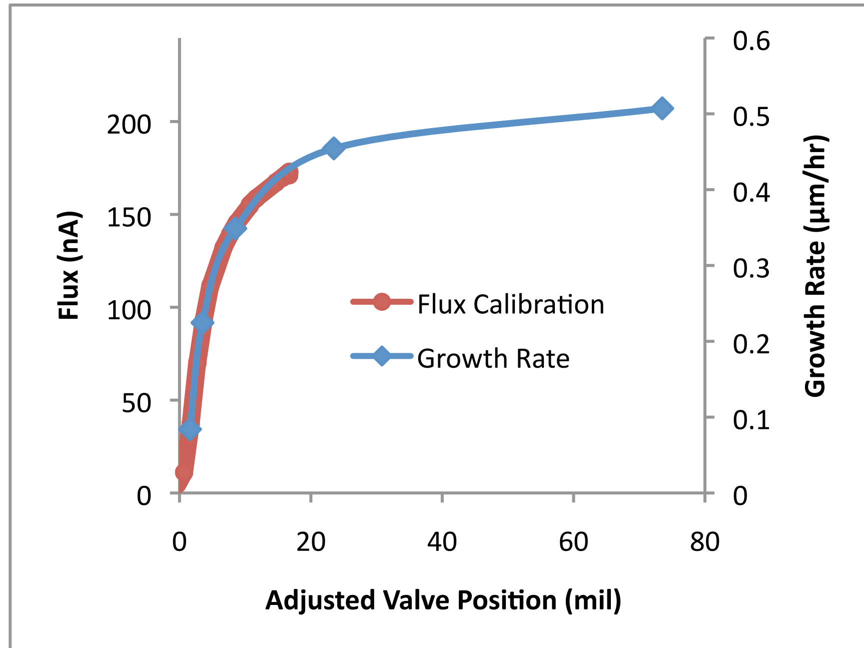

Figure 3.19: Growth rate versus Te valve position cross-section of Figure 3.18 at 418 °C superimposed on flux versus Te valve position from Figure 3.9.

Growth rates were obtained over a range of substrate temperatures for different Te valve settings (Figure 3.18). It is evident from the growth rate dependence on valve position that all characteristics were carried out under Zn-rich conditions. A cross-section of the plot in Figure 3.18 clearly shows that the Te-limited growth rate is directly proportional to the valve flux characteristic (Figure 3.19).

The growth rate versus substrate characteristic displays a negative slope from what appears to be an asymptote at low temperatures. At the upper end of the measured temperatures, the obtained data shows hints of the slope becoming significantly more negative. Measurements were attempted to continue the curve to higher temperature but significant degradation of the RHEED oscillations was

encountered. When the growth was interrupted, however, oscillations were observed. This was a result of layer-by-layer desorption in this regime. The rates of this action were obtained and are juxtaposed with the growth rate values in Figure 3.18. An exponential fit of these points shows a high level of correlation and offers a clear explanation of the noted temperature dependence.

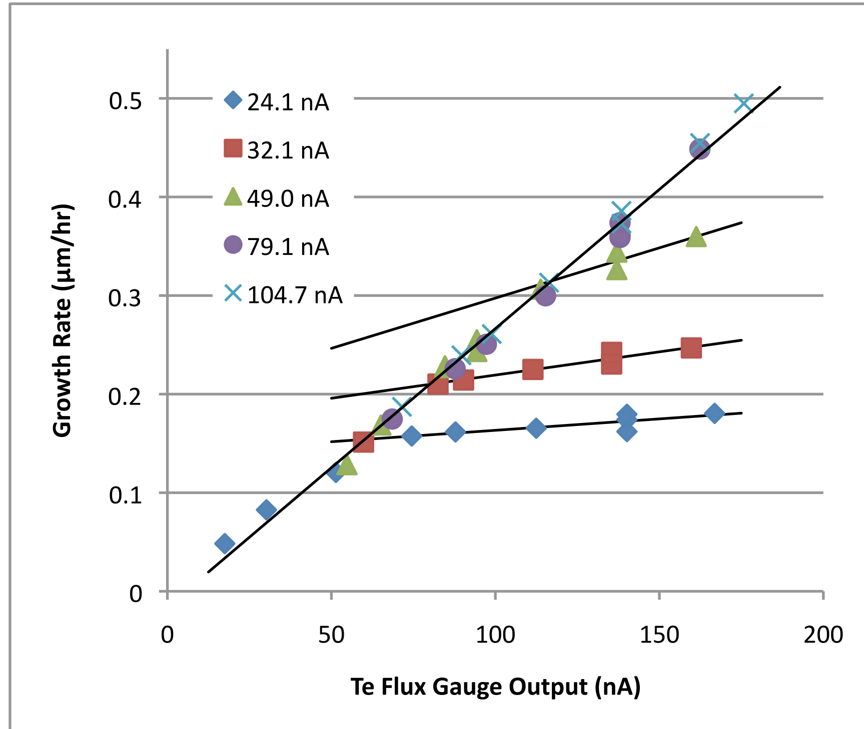

Figure 3.20: Growth rate versus measured Te flux for various Zn source fluxes.

It was expected that growth rate dependence would transition from the Te flux to the Zn flux if the latter was sufficiently lowered. This was tested by keeping a constant substrate temperature and varying the Te valve position for a set of Zn source temperature settings (Figure 3.20). A temperature of 385 °C was selected for its intermediate value and its oscillation reliability. During the measurement process, fluxes were obtained before and after each set of

measurements taken for a particular Zn flux setting. The midpoint at each valve setting is used in the plot and the variation between values was typically less then 5 percent.

The expected growth rate characteristic is clearly noted. At low values of Te flux, growth rate values for all Zn flux settings fall along the same positive linear relation confirming Te-limited growth. In the lower Zn flux curves, a significant and abrupt decrease in slope is noted signaling a transition to Zn limited growth. The Te flux level of this transition increases in order with increasing Zn flux levels.

Table 3.1: Fluxes resulting in stoichiometric adsorption with corresponding Te/Zn ratio

Zn Temperature (°C)	Zn Flux (nA)	Te Flux (nA)	Estimated 1:1 Flux Ratio (Te/Zn)	Measured Flux Ratio (Te/Zn)
350	24.1	60.2	1.76	2.50
360	32.1	80.0	1.79	2.49
375	49.0	117.1	1.83	2.39

This transition point indicates the conditions at which there is a stoichiometric ratio of adatoms at the sample surface. The Te flux value at which this occurs is extracted using the intersection of linear fits of the Zn-rich and Te-rich regions. These are shown along with the corresponding Zn flux and measured

ratio in Table 3.1. Since the ion gauge used for flux measurements has different sensitivities for Zn and Te, the true 1:1 flux ratio is estimated using

$$P_{Te}/P_{Zn} = [(J_{Te}\eta_{Te})/(J_{Zn}\eta_{Zn})][(T_{Zn}M_{Te})/(T_{Te}M_{Zn})]^{1/2}$$

where P represents the measured flux of a species, M is its molecular weight, T is the source temperature, and η is its ionization efficiency which can be estimated relative to nitrogen by

$$\eta_x/\eta(N_2) = 0.4Z/14 + 0.6$$

where Z is the atomic number [**20**]. Comparing the obtained values with the measured flux ratios indicates that a higher Te flux is required to reach stoichiometric adsorption. This suggests that Te has a lower comparative sticking coefficient at these conditions.

Beyond the stoichiometric condition, a small positive slope of the growth rate versus Te flux curve is observed. This is in violation of the first order hypothesis that this trend would become constant in accordance with the constant Zn flux. A potential explanation is that the Te excess at the surface increases the Zn sticking coefficient [**42**]. Subsequently, there is a corresponding increase in the amount of Zn available for incorporation into the crystal.

4 SUMMARY AND CONCLUSIONS

A dual chamber MBE system was rebuilt to enable the growth of 6.1 Å lattice-matched II-VI and III-V semiconductors. Alloys of this platform enable nearly complete coverage of the bandgap ranging from 0 eV to 3.4 eV. A number of optoelectronic applications have been proposed that take advantage of this property. High efficiency multijunction solar cells with four or more junctions and two terminal multicolor photodetectors are two examples.

In order to successfully grow devices such as these, an MBE system with low contaminant levels is needed. Achieving this for the II-VI chamber involved extensive cleaning procedures to remove deposited III-V materials. This began with physical removal methods followed by a 300 °C bake on the II-VI chamber to drive off remaining III-V contaminants. A comparison of residual gas analysis scans between the baked II-VI and III-V chamber confirmed a successful reduction of As and other contaminants.

In order to prevent further contamination, system components were either carefully cleaned or fully replaced. In particular, all pumps were rebuilt for this reason as well as to promote system reliability. Special features were added to the II-VI chamber to enable higher temperature bakes. These included the use of valved cells and the addition of a cold trap. Additional features were incorporated to increase the level of control attainable within the system. A high performance computer control system was implemented enabling programming of complex growth structures and also real time device control. Measurement and analysis

systems such as reflection-high energy electron diffraction, diffuse reflectance spectroscopy, and residual gas analysis were also implemented.

A full system bake carried out over a period of over two weeks and reaching up to 200 °C was used to remove contaminants from the upgrade process and exposure to atmosphere. This improved the system vacuum by over an order of magnitude which was reflected by the significant reduction of impurities as shown by residual gas analysis. Measures to reduce II-VI material outgassing were shown to be successful as only a small increase of the partial pressures of these elements was noted.

In this work, calibration and growth optimization of ZnSe and ZnTe was carried out. Each of the sources used in these materials displayed the expected exponential flux versus temperature characteristic. The flux versus valve position for both Se and Te displayed a high initial slope with asymptotic behavior as the fully open flux value was approached. Due to the high slope, frequent calibrations are required to achieve accurate flux output at intermediate valve positions.

GaAs substrates were used for the growth studies. Due to contamination constraints, an As-free deoxidation procedure was developed. Consistent results were achieved using a fast ramp to a substrate temperature of approximately 615 °C followed by a 1-4 minute hold during which RHEED was monitored for an increase in brightness and appearance of second order lines in the [110] direction.

ZnSe growths were carried out for a range of substrate temperatures. X-ray diffraction ω-2θ scans were used to analyze material quality. The data, carried out over a range of 278 °C to 400 °C, showed a trend of improving material as

temperature was decreased. Full-width half-maximum values as low as 113 arcsec confirm that the MBE system is capable of high quality growth.

A similar study was carried out for ZnTe. For this material, crystal quality increased with temperature up to 440 °C. It is believed that this increased the ability of adatoms to find energetically favorable sites helping to quickly alleviate strain induced by the 7.9% lattice mismatch with GaAs. A reasonably low FWHM of 84 arcsec was obtained, however significantly lower values have been published suggesting further optimization is possible [**18**].

The dependence of ZnTe growth rate on substrate temperature was studied using RHEED oscillation. A decrease in growth rate as temperature was increased was noted. This was shown to primarily correspond to an increase in desorption rates with temperature.

Similarly, RHEED oscillations were used to obtain growth rates for various flux conditions. It was shown that the stoichiometric growth condition could be located by varying the Te flux at different Zn fluxes. This occurred for Te to Zn ratios between 2.39 and 2.50. Beyond this point, a small slope in the growth rate versus Te flux curve at a fixed Zn flux level indicates that the Zn is incorporated more efficiently as the surface becomes more Te rich.

Overall, the rebuild of a dual chamber MBE system for the growth of 6.1 Å II-VI and III-V materials has proven successful. Extensive contaminant reduction and new system features have fostered the ability to grow high quality materials. Paths for further optimization have been identified and it is expected that this will soon enable exploration into novel device concepts that take full

advantage of the unique properties of the 6.1 Å II-VI and III-V materials platform.

REFERENCES

[1] Y.-H. Zhang, S.-N. Wu, D. Ding, S.-Q. Yu, and S. R. Johnson, "A Proposal of Monolithically Integrated Solar Cells Using Lattice-Matched II/VI and III/V Semiconductors," in *Proceeding of the 33rd IEEE Photovoltaic Specialists Conference*, San Diego, CA, 2008.

[2] C. H. Henry, "Limiting efficiencies of ideal single and multiple energy gap terrestrial solar cells," *Journal of Applied Physics*, 1980.

[3] W. Shockley and H. J Queisser, "Detailed Balance Limit of Efficiency of p-n Junction Solar Cells," *Journal of Applied Physics*, vol. 32, no. 3, p. 510, March 1961.

[4] (2012, February) National Renewable Energy Laboratory. [Online]. http://www.nrel.gov/ncpv/images/efficiency_chart.jpg

[5] R. R. King, D. C. Law, K. M. Edmondson, C. M. Fetzer, G. S. Kinsey, H. Yoon, D. D. Krut, J. H. Ermer, R. A. Sherif, and N. H. Karam, "Advances in High-Efficiency III-V Multijunction Solar Cells," *Advances in Optoelectronics*, 2007.

[6] (2011, August) Compound Semiconductor. [Online]. http://www.compoundsemiconductor.net/csc/features-details.php?cat=news&id=19733899&name=Dilute%20nitrides%20give%20Solar%20Junction%20a%20critical%20edge

[7] S-.N. Wu, D. Ding, S. R. Johnson, and Y.-H. Zhang, "Four-junction solar cells using lattice-matched II–VI and III–V semiconductors," *Progress in Photovoltaics: Research and Applications*, no. 18, pp. 328-333, April 2010.

[8] E. H. Steenbergen, M. J. DiNezza, W. H. G. Dettlaff, S. H. Lim, and Y.-H. Zhang, "Optically-addressed two-terminal multicolor photodetector," *Applied Physics Letters*, vol. 97, no. 16, pp. 161111-161111-3, October 2010.

[9] E. H. Steenbergen, M. J. DiNezza, W. H. G. Dettlaff, S. H. Lim, and Y.-H. Zhang, "Effect of varying light bias on an optically-addressed two-terminal multicolor photodetector," *Infrared Physics and Technology*, vol. 54, pp. 292-295, 2011.

[10] E. F. Schulte, "Two Terminal Multi-Band Infrared Radiation Detection,"

U.S. Patent 5113,076, May 12, 1992.

[11] E. R. Blazejewski, J. M. Arias, G. M. Williams, W. McLevige, M. Zandian, and J. Pasko, "Bias-switchable dual-band HgCdTe infrared photodetector," *Journal of Vacuum Science and Technology B*, vol. 10, p. 1626, 1992.

[12] J. C. Campbell, T. P. Lee, A. G. Dentai, and C. A. Burrus, "Dual-wavelength demultiplexing InGaAsP photodiode ," *Applied Physics Letters*, vol. 34, p. 401, 1979.

[13] K. Kosai, "Three Band and Four Band Multispectral Structures having Two Simultaneous Signal Outputs," U.S. Patent 5731,621, March 24, 1998.

[14] T. Chu, "Multi-color Coincident Infrared Detector," U.S. Patent 5059,786, October 22, 1991.

[15] A. Rogalski, "New material systems for third generation photodetectors," *Opto-Electronics Review*, vol. 26, no. 4, pp. 458-482, 2008.

[16] S. Adachi, *Handbook on Physical Properties of Semiconductors*.: Springer-Verlag, 2004.

[17] S. Wang, D. Ding, X. Liu, X.-B. Zhang, D. J. Smith, J. K. Furdyna, and Y.-H. Zhang, "MBE growth of II-VI materials on GaSb substrates for photovoltaic applications," *Journal of Crystal Growth*, vol. 311, p. 2116, 2009.

[18] J. Fan, L. Ouyang, X. Liu, D. Ding, D. J. Smith, and Y.-H. Zhang, "Growth and material properties of ZnTe on GaAs, InP, InAs, and GaSb (0 0 1) substrates for electronic and optoelectronic device applications," *Journal of Crystal Growth*, vol. 323, p. 127, 2011.

[19] N. Magnea, "Optical identification of substitutional acceptors in refined ZnTe," *Physica status solidi. B, Basic research*, vol. 94, no. 2, p. 627, August 1979.

[20] M. A. Herman and H. Sitter, *Molecular Beam Epitaxy: Fundamentals and Current Status*, 2nd ed. New York: Springer, 1996.

[21] R. C. Farrow, Ed., *Molecular Beam Epitaxy*. Park Ridge, NY: Noyes Publications, 1995.

[22] Kurt J. Lesker Company. [Online]. http://www.lesker.com/newweb/Vacuum_Pumps/vacuumpumps_technicalnotes_1.cfm

[23] S. Tixier, M. Adamcyk, E. C. Young, J. H. Schmid, and T. Tiedje, "Surfactant enhanced growth of GaNAs and InGaNAs using bismuth," *Journal of Crystal Growth*, vol. 251, no. 1-4, p. 449, 251 2003.

[24] N. A. Riordan, C. Gogeneni, S. R. Johnson, X. Lu, T. Tiedje, D. Ding, Y.-H. Zhang, R. Fritz, K. Kolata, S. Chatterjee, K. Volz, and S. W. Koch, "Temperature and pump power dependent photoluminescence characterization of MBE grown GaAsBi on GaAs," *Journal of Materials Science: Materials in Electronics*, March 2012.

[25] S. R. Johnson, C. Lavoie, T. Tiedje, and J. A. Mackenzie, "Semiconductor substrate temperature measurement by diffuse reflectance spectroscopy in molecular beam epitaxy," *Journal of Vacuum Science and Technology*, vol. 11, no. 3, p. 1007, 1993.

[26] J. M. Bellama and A. G. MacDiarmid, "Synthesis of the Hydrides of Germanium, Phosphorus, Arsenic, and Antimony by the Solid-Phase Reaction of the Corresponding Oxide with Lithium Aluminum Hydride," *Inorganic Chemistry*, vol. 7, p. 2070, 1968.

[27] Occupational Health & Safety Admnistration. [Online]. http://www.osha.gov/pls/oshaweb/owadisp.show_document?p_table=STANDARDS&p_id=9992&p_text_version=FALSE

[28] P. Walker and W. H. Tarn, Eds., *Handbook of Metal Etchants*. Boca Raton, FL, USA: CRC Press, 1991.

[29] V. Bousquet, C. Ongaretto, M. Laught, M. Behringer, E. Tournie, and J. P. Faurie, "(001) GaAs substrate preparation for direct ZnSe heteroepitaxy," *Journal of Applied Physics*, vol. 81, no. 10, p. 7012, May 1997.

[30] H. J. Cornelissen, D. A. Cammack, and R. J. Dalby, "Reflection high-energy electron diffraction observations during growth of ZnSxS(1-x) (0≤x≤1)) by molecular-beam epitaxy," *Journal of Vacuum Science and Technology B*, vol. 6, no. 2, p. 769, Mar/Apr 1988.

[31] C. R. Li, B. K. Tanner, D. E. Ashenford, J. H. C. Hogg, and B. Lunn, "High resolution x-ray diffraction and scattering measurement of the interfacial structure of ZnTe/GaSb epilayers ," *Journal of Applied Physics*, vol. 85, no.

10, p. 2281, September 1997.

[32] K. Menda, I. Takayasu, T. Minato, and M. Kawashima, "RHEED Observation on (001)ZnSe Surface: MBE Surface Phase Diagram and Kinetic Behavior of Zn and Se Adatoms," *Japanese Journal of Applied Physics*, vol. 26, no. 8, p. 1326, Aug 1987.

[33] P. Ruppert, D. Hommel, T. Behr, H. Heinke, A. Waag, and G. Landwehr, "Molecular beam epitaxial growth mechanism of ZnSe epilayers grown on (100) GaAs as determined by reflection high-energy electron diffraction, transmission electron diffraction, and X-ray diffraction," *Journal of Crystal Growth*, vol. 138, p. 48, 1994.

[34] J. S. Song, J. H. Chang, D. C. Oh, J. J. Kim, M. W. Cho, H. Makino, T. Hanada, and T. Yao, "Optimization of ZnSe growth on miscut GaAs substrates by molecular beam epitaxy," *Journal of Crystal Growth*, vol. 249, p. 128, 2003.

[35] J.M. Gaines, J. Petruzzello, and B. Greenberg, "Structural properties of ZnSe films grown by migration enhanced epitaxy," *Journal of Applied Physics*, vol. 73, no. 6, p. 2835, 1993.

[36] J. E. Ayers, "The measurement of threading dislocation densities in semiconductor crystals by X-ray diffraction," *Journal of Crystal Growth*, vol. 135, p. 71, 1994.

[37] S. Tatarenko, B. Daudin, and D. Brun-Le Cunff, "Zn and Te Desorption from the (100) ZnTe surface," *Applied Physics Letters*, vol. 66, no. 13, p. 1773, April 1995.

[38] W. Lee, M. Jung, M. Jung, H. Lee, S. Lee, S. Park, T. Yao, J. Song, H. Ko, and J. Chang, "Structural deformation reduction of ZnTe heteroepitaxial layers grown on GaAs (0 0 1) substrate by using low-temperature buffer," *Journal of Crystal Growth*, vol. 304, p. 22, 2007.

[39] J. Zhao, Y. Zeng, C. Liu, and Y. Li, "Substrate temperature dependence of ZnTe epilayers grown on GaAs(0 0 1) by molecular beam epitaxy," *Journal of Crystal Growth*, vol. 312, p. 1491, 2010.

[40] R. D. Feldman, R. F. Austin, P. M. Bridenbaugh, A. M. Johnson, B. A. Wilson, and C. E. Bonner, "Effects of the Zn to Te ratio on the molecular-beam epitaxial growth of ZnTe on GaAs," *Journal of Applied Physics*, vol. 64, no. 3, p. 1191, August 1988.

[41] J. E. Ayers, "The measurement of threading dislocation densities in semiconductor crystals by X-ray diffraction," *Journal of Crystal Growth*, vol. 135, p. 71, 1994.

[42] R. Najjar, R. Andre, H. Boukari, H. Mariette, and S. Tatarenko, "Intensity beats on RHEED oscillations during MBE growth of ZnTe," *Surface Science*, vol. 602, p. 744, 2008.

[43] J. Zhao, Y. Zeng, C. Liu, L. Cui, and Y. Li, "Optimization of the II-VI pressure ratio in ZnTe growth on GaAs(0 0 1) by molecular beam epitaxy," *Applied Surface Science*, vol. 256, p. 6881, 2010.

[44] J. Riley, D. Wolfframm, D. Westwood, and A. Evans, "Studies in the growth of ZnSe on GaAs(001)," *Journal of Crystal Growth*, vol. 160, p. 193, 1996.